This is a repository copy of *Photoluminescent and superparamagnetic reduced graphene oxide-iron oxide quantum dots for dual-modality imaging, drug delivery and photothermal therapy*.

White Rose Research Online URL for this paper:
http://eprints.whiterose.ac.uk/97582/

Version: Accepted Version

Takedown

If you consider content in White Rose Research Online to be in breach of UK law, please notify us by emailing eprints@whiterose.ac.uk including the URL of the record and the reason for the withdrawal request.

Photoluminescent and superparamagnetic reduced graphene oxide-iron oxide quantum dots for dual-modality imaging, drug delivery and photothermal therapy

Richard Justin,[1] Ke Tao,[2] Sabiniano Román,[1] Dexin Chen,[2] Yawen Xu,[3] Xiangshuai Geng,[1] Ian M. Ross,[4] Richard T. Grant,[5] Andrew Pearson,[5] Guangdong Zhou,[3] Sheila MacNeil,[1] Kang Sun,*[2] and Biqiong Chen*[1]

[1]Department of Materials Science and Engineering, University of Sheffield, Mappin Street, Sheffield S1 3JD, United Kingdom.

[2]The State Key Laboratory of Metal Matrix Composites, School of Materials Science and Engineering, Shanghai Jiao Tong University, Shanghai 200240, China.

[3]Shanghai Key Laboratory of Tissue Engineering Research, National Tissue Engineering Center of China, Shanghai 200241, China.

[4]Department of Electronic and Electrical Engineering, University of Sheffield, Mappin Street, Sheffield S1 3JD, United Kingdom.

[5]Department of Physics and Astronomy, University of Sheffield, Hounsfield Road, Sheffield S3 7RH, United Kingdom

*Corresponding Author.

E-mail: biqiong.chen@sheffield.ac.uk; ksun@sjtu.edu.cn

Fax: +44 (0) 114 222 5943;

Tel: +44 (0) 114 222 5958.

Abstract

Reduced graphene oxide - iron oxide quantum dots (QDs) with intrinsic photoluminescent and superparamagnetic properties were synthesized through a green, hydrothermal method that simultaneously reduced and shattered graphene nanosheets to form the dots. The structure, morphology, properties and cell viability of these QDs were investigated. The QDs emitted violet light when excited at 320 nm, possessed no residual magnetization upon magnetic hysteresis tests, and had low cytotoxicity to healthy cells at low concentrations. The suitability of the QDs for fluorescent and magnetic resonance dual-modality imaging was shown by *in vitro* imaging with dermal fibroblast cells and T2 relaxation time. A drug could be loaded onto the surface of the QDs, with a loading ratio of drug to QD of 0.31:1. The drug achieved a steady but full release from the QDs over 8 h: these drug-loaded QDs could be manipulated by an external magnetic stimulation for targeted drug delivery. The potential for use as a cancer photothermal therapy was demonstrated by both a rapid, ~50 ^{o}C temperature increase by a suspension of 100 µg ml^{-1} of QDs and the photothermal ablation of HeLa cells *in vitro* under near infrared irradiation. The stability of the MGQDs in fetal calf serum was shown to improve when an ionic drug was coated on the surface.

1. Introduction

Biomedical technology is undergoing a period of rapid development, and one of the keys to this advancement is nanotechnology [1]. Graphene, and its chemically oxidized derivative graphene oxide (GO), have been investigated for drug delivery, biosensing, and cancer photothermal therapy as they have a large surface area, ample functional groups on the surface, photothermal properties and/or low cytotoxicity [2,3]. Iron oxide (IO) nanoparticles have also been studied for biomedical purposes [4]. Their superparamagnetic (i.e. they hold no residual magnetic force and can be manipulated by external magnetic fields) behavior allows for them to be used for targeted therapeutic delivery [5]. They can be imaged *in vivo* by Magnetic Resonance Imaging (M.R.I.), enabling the visualisation of tumors and the circulatory system, as well as finding use in magnetic hyperthermia [6,7].

IO can be deposited onto GO to form GO-IO or reduced graphene oxide (rGO)-IO hybrids [8–11] (the chemical deposition may reduce GO to rGO during the synthesis [12]), which can combine the interesting aspects of both individual nanoparticles [8–12]. Previous work [9,12] has shown that graphene-IO nanoparticles can be used for targeted drug delivery, M.R.I., and photothermal therapy; the functional groups of GO or rGO allow for drug loading while the superparamagnetic properties of IO enable the hybrids to be used for targeted drug delivery using an external magnetic stimulus and M.R.I.. Both graphene [13] and IO [14] were shown to absorb near infrared (NIR) light, which was converted into heat for photothermal therapy. For instance, GO-IO reduced the cancer cell viability by ~90% by using a 2 W cm^{-2} laser for 5 min [9], and rGO-IO achieved the full ablation of tumours within mice within 24 h using a 0.5 W cm^{-2} laser as the irradiation source [12]. However, no intrinsic photoluminescent properties were demonstrated for the graphene – IO nanoparticles reported in the literature [11,15,16]. The fluorescent imaging capability of the rGO-IO nanoparticles were from dyes (polyfluorene [11] and cyanine [12]) bonded to the nanoparticle surface. The photoluminescent properties of the GO-IO were attributed to the bonded doxorubicin, which the GO-IO quenched in comparison to free doxorubicin [9]; these nanoparticles were approximately 50 – 300 nm in size and did not possess intrinsic photoluminescent properties.

Quantum dots (QDs) emit a luminescence due to quantum confinement effects [17]. Conventionally, QDs were made of compounds like cadmium selenide (CdSe) or cadmium telluride (CdTe), but they were found to be cytotoxic during *in vitro* cell tests due to the photolysis release of cadmium ions and the uncoiling of DNA helical strands [18,19]. This led to the development of biocompatible carbon-based QDs, with QDs derived from carbohydrates [20], nanodiamonds [21], and graphene [22–25]. Graphene QDs (GQDs) can

be created by ultrasonication [22], chemical reduction [23], photo-reduction [24], and hydrothermal cutting [25]. These carbon QDs emit the same level of luminescence as the cadmium QDs, but do not carry the same cytotoxic risk. It has been shown that GQDs could enter cells but did not enter the nucleus of stem cells during *in vitro* tests; they maintained a high (80%) viability for neurosphere and pancreas progenitor cells up to 100 µg ml^{-1} after 72 h [26], and carboxylated GQDs caused no acute toxicity to rats after 22 days post injection at a concentration of 10 mg kg^{-1} [27]. Carbon QDs can be excreted rapidly from the body after being administered through intravenous, intramuscular or subcutaneous injections [28].

To the authors' knowledge, biocompatible graphene-based magnetic QDs that are intrinsically both superparamagnetic and photoluminescent have not yet been reported. Quantum dots with magnetic properties (MQDs) can by synthesized by either doping conventional QDs (for example CdSe, or CdTe) with metal elements like manganese [29], nickel [30], or gadolinium [31], or by encasing conventional QDs with IO [32] in silica spheres. These MQDs possess the photoluminescent properties of conventional QDs and the magnetic properties of the doping agent or the encapsulated IO, but they contain cytotoxic compounds such as cadmium selenium or cadmium telluride and are therefore cytotoxic without a biocompatible passivation coating [30]. The aim of this work was to synthesize magnetic graphene-IO quantum dots (herein MGQDs) as a multifunctional nanosystem for fluorescent imaging, M.R.I., targeted drug delivery and photothermal therapy for concurrent detection, monitoring and treatment of diseases. The MGQDs were synthesized by depositing IO on GO surface, followed by autoclaving to reduce GO into rGO and form the MGQDs. Their structure, morphology, cell viability, drug release behavior, fluorescent imaging and M.R.I. capabilities and photothermal properties were assessed.

2. Experimental

2.1 Materials

The following chemicals were used as purchased from Sigma Aldrich; sulfuric acid (95-98%), hydrogen peroxide (29-32% in water), potassium permanganate (97%), sodium nitrate (> 99%), ferrous chloride tetrahydrate (> 99%), hydrochloric acid (36.5%), ferric chloride hexahydrate (97%), fluorescein sodium, graphite powder (≤ 20 µm), rhodamine B, norharmane, lidocaine hydrochloride (> 99%), porcine trypsin (BioReagent), 3-[4,5-dimethylthiazol-2-yl]-2,5-diphenyltetrazolium bromide (MTT) solution (1 mg ml^{-1} in phosphate buffered saline (PBS)), and ethylenediaminetetraacetic acid (EDTA, BioReagent). Dulbecco's modified eagle medium (DMEM, 500 ml, Gibco Invitrogen (Paisley, UK) was

4

used with fetal calf serum (FCS, Advanced Protein Products, Brierley Hill, UK), penicillin (100 units ml^{-1}), streptomycin (100 µg ml^{-1}), and fungizone (630 ng ml^{-1}) from Gibco Invitrogen (Paisley, UK). Isopropanol alcohol (reagent grade) and PBS tablets (pH = 7.4) were acquired from Fisher Scientific UK.

2.2 Preparation of graphene oxide – iron oxide nanoparticles

Graphene oxide was synthesized from a modified Hummers method [33] and GO-IO was prepared according to methods described in the literature with some modifications [8,34]. The freeze-dried GO powder (1 g) was dispersed in 150 ml of distilled water through stirring and sonication for 1 h and the pH of the suspension was raised to pH = 8 with the addition of ammonium hydroxide NH_4OH. Separately, ferrous chloride tetrahydrate $FeCl_2$-$4H_2O$ (5.4 g) and ferric chloride hexahydrate $FeCl_3$-$6H_2O$ (4 g) were dissolved in 135 ml distilled water. The GO suspension and the solution of IO precursors were added together, ammonium hydroxide was added drop wise until a pH = 10 was reached, and then the mixture was stirred for 2 h under a nitrogen atmosphere at ambient temperature. The precipitate, iron oxide coated graphene oxide (GO-IO), was washed with distilled water, ethanol and dichloromethane to remove residual chemicals, separated from unbound, hydrophobic IO precipitate by decanting the GO-IO as the supernatant from an aqueous suspension, before being re-dispersed in distilled water (~ 3 mg ml^{-1}) by sonication for 1 h in a Fisherbrand sonication bath (230 V, 50-60 Hz). As a control sample, IO was prepared using the same method but without the addition of GO.

2.3 Preparation of reduced graphene oxide-iron oxide quantum dots

The aqueous GO-IO suspension (~ 3 mg ml^{-1}) was treated in a Parr Series 4000 autoclave at 200 ^{o}C for 10 h (pressure of boiling water at 201 ^{o}C = 1.6 MPa) to generate reduced graphene oxide-iron oxide quantum dots (namely, MGQDs). The suspension was placed in a dialysis bag (Fisher Scientific Biodesign Dialysis tubing, molecular weight cut off = 3.5 kDa) and the residual chemicals were allowed to diffuse into the distilled water surrounding the dialysis bag [25]. The MGQDs were collected in an aqueous suspension from the dialysis bag and lyophilized in a Labconco FreeZone Triad freeze-dryer to be stored as a powder in a desiccator. As a control, GO and IO (both with a raised pH of 8) were autoclaved at 200 ^{o}C for 10 h to produce graphene quantum dots and autoclaved iron oxide (A-IO) for a comparison study.

2.4 Drug loading onto quantum dots

Lidocaine hydrochloride (LH) (0.1 mg ml^{-1}) was added to a 100 ml suspension of MGQDs (0.1 mg ml^{-1}) under stirring for 48 h. The suspension was centrifuged at 9000 rpm for 1 hour, after which the supernatant (containing unbound LH) was removed and the precipitate was re-dispersed in water. This process was repeated several times to remove all of the unbound LH. The MGQD-LH was then freeze-dried and stored in a desiccator.

2.5 Characterization

Transmission electron microscopy (TEM), energy dispersive X-ray spectroscopy (EDS), and selected area electron diffraction (SAED) were achieved using a Philips Technai T20 electron microscope operating at an accelerating voltage of 200 kV. High resolution TEM (HR-TEM) was carried out using a JEOL 2010F field emission gun TEM operating at an accelerating voltage of 200 kV. TEM and HR-TEM samples were prepared by evaporating a diluted suspension (~ 0.01 mg ml^{-1}) onto a holey amorphous carbon coated copper grid (mesh size = 400). Electron energy loss spectroscopy (EELS) spectra were acquired on the JEOL 2010F using a Gatan image filter in image coupled mode with an energy dispersion of 0.5 eV per pixel. Atomic force microscopy (AFM) was carried out on a Veeco Dimension 3100 with Olympus AC160TS probes in tapping mode at 0.5 Hz, using a diluted suspension (~ 0.01 mg ml^{-1}) evaporated onto a freshly cleaved mica substrate. Dynamic light scattering (DLS) was performed on a Brookhaven ZetaPALS (660 nm wavelength), with 3 cycles of 2 min runs on suspensions of 1 mg ml^{-1} MGQD in distilled water.

X-ray diffraction (XRD) was performed on a Stoe Stadi P with Cu K$_\alpha$ irradiation (0.154 nm wavelength), with operating parameters of 40 kV, 35 mA, and a scanning speed of 1° min^{-1}. Raman spectroscopy between 50-3000 cm^{-1} with a resolution of 0.5 cm^{-1} was achieved with a Renishaw inVia Raman microscope using a 514.5 nm wavelength laser. Fourier transform infrared (FT-IR) spectroscopy between 400-4000 cm^{-1} with a resolution of 1 cm^{-1} was performed on a Perkin Elmer Spectrum 100 with a diamond attenuated total reflectance unit. Thermogravimetric analysis (TGA) was implemented on a Perkin Elmer Pyris 1 with a nitrogen atmosphere (20 ml min^{-1}) at a heating rate of 5 ^{o}C min^{-1}. Inductively coupled plasma mass spectrometry (ICP-MS) was carried out using a Spectro-Ciros-Vision ICP-Emission Spectrometer. Samples were extracted in 12 ml aqua regia at 150 ^{o}C for 30 min, followed by the addition of 1 ml hydrofluoric acid and stirring at 150 ^{o}C for 15 min, and were then diluted using distilled water to a total end volume of 50 ml. A Micromeritics AccuPyc II 1340 was used to measure the density of the MGQDs, achieved at room temperature (24 ^{o}C) by using 10 purge cycles and 10 calculation cycles of helium gas.

UV-visible light (UV-Vis) spectroscopy of nanoparticle suspensions in distilled water (0.3 mg ml^{-1} concentration) from 200-800 nm with a 1 nm resolution was achieved with a Perkin Elmer Lambda 900 spectrometer. Photoluminescence spectroscopy was conducted using a Horiba Fluoromax 4 with excitation sources from 300-400 nm and emission readings from 360-600 nm with a wavelength resolution of 2 nm. Photoluminescence quantum yield measurements used fluorescein sodium in 0.1 NaOH, rhodamine B in ethanol and 0.01% HCl, and norharmane in 0.1 M H$_2$SO$_4$ as reference standards. Quantum yield measurements were taken by using Equation 1 [35], shown below:

$$\phi_{qd} = \phi_{st} \times \frac{Grad_{qd}}{Grad_{st}} \times \frac{\eta_{qd}^2}{\eta_{st}^2} \qquad (1)$$

where "ϕ" is the fluorescence quantum yield, "Grad" is the gradient of the curve of emission versus absorbance, "η" is the refractive index for the solvent used in the solution, and "qd" and "st" are quantum dots and the standards used (fluorescein sodium, rhodamine B and norharmane). PL lifetime analysis (time correlated single photon counting) was achieved with irradiation from a frequency doubled Mira 900 Ti-Sapphire laser (10 W), a single photon counting module (Becker and Hickl SPC-830), an electronic trigger (Becker & Hickl GmbH PHD-400-N High Speed Photodiode Module), and the emission was detected by an ID Quantique ID100-50 single photon detection module. The magnetic hysteresis loop was created using a Quantum Design MPMS-XL 5 superconducting quantum interference device (SQUID), operating at 37 °C to simulate *in vivo* conditions and between +/- 20,000 Oe (2 T) in 200 Oe intervals. A Siemens Trio TIM 3 Tesla M.R.I. was used to measure the T2 relaxation times of the MGQDs, with the echo time, T_E = 15.2, 30.4, 45.6, 60.8, 76, 91.2, 106.4, 121.6, 136.8, 152, 167.2 milliseconds and the relaxation time T_R = 3000 milliseconds.

2.6 Cell viability and imaging

Human skin was obtained with ethical permission from patients undergoing abdominoplasties or breast reductions from the Department of Plastics, Burns and Reconstructive Surgery, Sheffield Teaching Hospitals. All tissue was collected and used on an anonymous basis under a Human Tissue Authority research bank tissue license number 08/H1308/39.

Dermal fibroblast cells were isolated and cultured, as described previously [36], in DMEM at 37 °C and 5% CO$_2$ environment. When the culture was 50% confluent, the cells were collected by treating with a trypsin solution for 10 min and centrifuging the cell suspension to form a pellet at 1000 rpm for 5 min using a Hettich Rotafix 32A centrifuge. Cells were counted, with cells seeded (10,000 per well) in a 48 well plate. Cells were incubated overnight in DMEM to allow for cell reattachment, after which the DMEM medium was replaced with MGQD suspensions (20, 50, 100, 200, 500 µg ml^{-1} in DMEM) for

6 and 24 h incubation times (each testing iteration was tested in triplicate). At the end of each incubation time, cells were washed with PBS and then incubated in fresh DMEM until 72 h post-treatment when cells were assessed by the MTT-assay of metabolic activity. Cells were incubated for 40 min at 37 $^{\circ}$C, after which the formazan salt was eluded by acidified isopropanol. The optical densities of the resultant solutions were measured with a plate reader at 540 nm with a reference filter of 630 nm (Bio-Tek ELx800). Control samples of untreated cells in DMEM were taken as 100% viable, and the optical densities of the MGQD treated cells were compared to these values.

An Olympus CK40 microscope and a Leica TCS SP8 two-photon confocal microscope (excitation source 690 nm, emission filter 360 nm) were used for cell imaging. For the two-photon fluorescent imaging, the cells were incubated with either 50 µg ml^{-1} or 100 µg ml^{-1} MGQDs for 12 h before the cells were fixed with glutaraldehyde.

2.7 Drug release from MGQDs

A 10 ml PBS suspension (37 $^{\circ}$C, pH = 7.4) of MGQD-LH (1 mg ml^{-1} MGQD-LH) was inserted into a Spectrum Labs Float-A-Lyzer G2 dialysis tube with pore sizes between 0.1 – 0.5 kDa. This dialysis tube was floated vertically in a sealed container of pristine PBS solution (550 ml, 37 $^{\circ}$C, pH = 7.4), with a float at the top and a weight at the end maintaining the buoyancy of the dialysis tube just under the surface of the solution. This container was placed within a Stuart SI500 bio-incubator, maintained at 37 $^{\circ}$C and agitated at 100 rpm. At set time points, 3 ml of PBS solution was taken from the outer container (replaced with 3 ml of fresh PBS) and analyzed with a Perkin Elmer Lambda 900 (resolution of 1 nm). The acquired spectra were compared to the absorbance values of free LH of known concentration (ranging from 0.06 – 1 mg ml^{-1}) in PBS.

2.8 Photothermal measurements

The temperature of aqueous suspensions of MGQDs and GQDs (1.5 ml, concentration of 50 µg ml^{-1} and 100 µg ml^{-1}) under irradiation from a near-infrared continuous laser (wavelength: 808 nm; laser power: 2, 5, 7.5 W cm^{-2}) was measured as a function of time. Distilled water was studied as a control.

Photothermal experiments on HeLa cells incubated with suspensions of MGQDs and GQDs were carried out with a near-infrared continuous laser (wavelength: 808 nm; laser power: 2.5 W cm^{-2}). HeLa cells were seeded to a density of 5000 cells per well of a 96 well culture plate (BD Falcon, U.S.). Cells were incubated at 37 $^{\circ}$C in a 5% CO_2 atmosphere for 24 h to allow for reattachment. After incubation, the cell culture medium was replaced by the MGQD or GQD suspension (100 µl of cell medium with a 50 µg ml^{-1} suspension of MGQD

or GQD). After 4 h incubation with the QDs, the cells were irradiated by a laser for 20 min or 30 min. After incubation overnight, the QD suspension medium was removed and the cells were washed twice with PBS. To test the viability of the cells after irradiation, 100 μl of CCK-8 solution was added to each well and the cells were incubated for 2 h. The optical density of the cell solution was read on a microplate reader (Varioskan Flash, Thermo Scientific), with measurements taken at 450 nm.

2.9 Biostability

MGQD and MGQD-LH were dispersed in distilled water, PBS and FCS at a concentration of 50 μg ml^{-1}. Suspensions were imaged using a digital camera after predetermined intervals.

2.10 Statistical analysis

Statistical analysis ($p < 0.05$) and graphing were completed through MatLab 2012a software. Size analysis of TEM images was conducted through ImageJ software, with 60 separate samples taken over several images.

3. Results and discussion

3.1 Structure

MGQDs were synthesized by coating the surface of GO with IO using the precursors of IO, followed by a hydrothermal treatment to simultaneously reduce GO into rGO and shatter the nanosheets to form MGQDs. The synthesis procedure is illustrated in Figure 1. Figure 2A shows TEM (A-1 and A-2) and AFM (Fig. 2B, Inset) images of MGQDs. The synthesized MGQDs have an average diameter of 41.8 (±8.1) nm from the TEM images, and an average diameter of 45.2 (±10.3 nm) and a height of 2.3 nm (±0.07 nm) from AFM. DLS results (Fig. 2B) show a mean hydrodynamic diameter of 61.4 nm, with a significant count within the 45–90 nm range. It is larger than the average diameters obtained from AFM and TEM, which can be accounted for by the presence of larger nanoparticles (i.e. agglomerates) in the polydisperse MGQD water suspension [37]. The diameter of the MGQDs is larger than hydrothermally reduced GQDs (5–25 nm) previously reported by by other groups [25,38,39], but these papers use either a longer hydrothermal treatment time (24 h) [38,39] or an additional oxidation procedure to further reduce the size of their GO before the hydrothermal treatment [25]. The diameter is, however, similar to that of the GQDs (51.9 nm) prepared by the same oxidation and hydrothermal treatment method in our group [40].
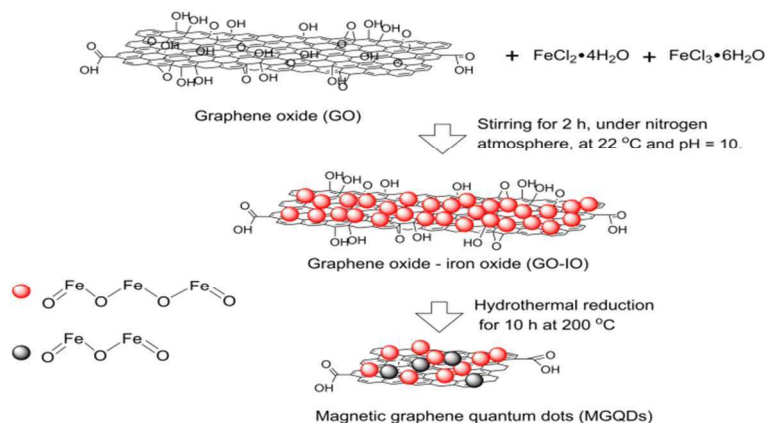
**Figure 1** Synthesis procedure for magnetic graphene quantum dots (MGQDs).
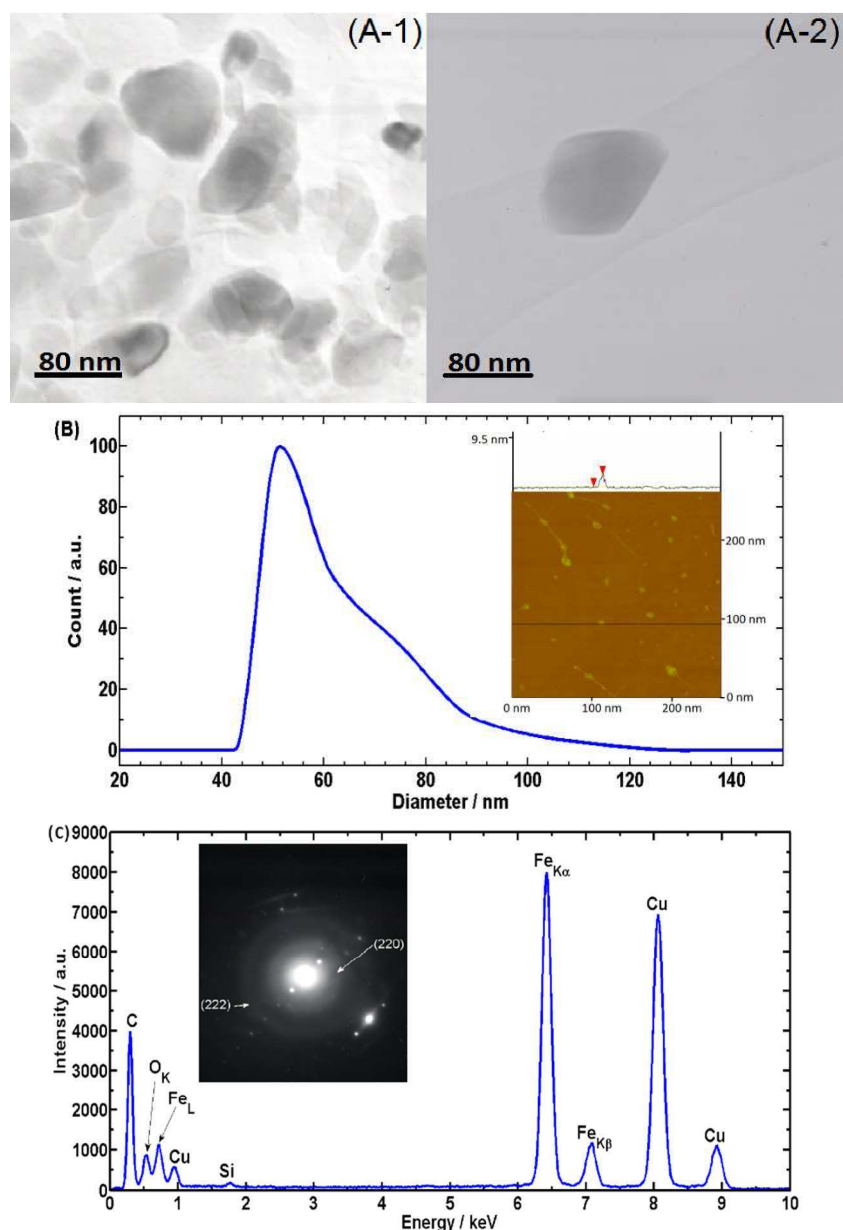
Figure 2 (A) TEM images of MGQDs, showing that the QDs are approximately 40-50 nm in diameter, (B) DLS size analysis of MGQD aqueous suspension, showing the majority of MGQDs are within the 45-90 nm diameter range; (Inset) AFM image of MGQDs, showing an average height of 2.3 nm and an average width of 45.2 nm. (C) EDS spectrum of the MGQD presented in Figure 2 (A-2), showing a composition of carbon, oxygen, and iron; (inset) the SAED pattern of the MGQD, confirming the presence of iron oxide.

The MGQDs are identifiable in both the conventional and high resolution TEM images in dark contrast (Figure 2A1-2A2, 3A) on the amorphous carbon film support due to the presence of high density IO (4.9 – 5.2 g cm^{-3} for magnetite [41]) within the MGQDs as well as mass-thickness contrast, similar to the identification of IO on GO-IO reported in the literature [9]. Under HR-TEM, a region of magnetite (Fe$_3$O$_4$) within an MGQD (Figure 3B) can be identified by the (400) lattice spacing ~0.227 nm [42], with a similar region of magnetite in Figure 3C, 3D and 3E identifiable by the (220) lattice spacing of ~0.345 nm [42,43]. A region of folded graphene (or rGO) layers can also be seen in Figure 3D and 3E by the (002) lattice spacing of ~0.347 nm and the wrinkled structure similar to the literature [44,45]. The region of graphene in Figure 3D and 3E contrasts in structure to the amorphous carbon support on the TEM grid, shown in Figure S1 of Supplemental Information and also present in the upper section of Figure 3C. The region of IO in Figure 3D and 3E appears to be on the surface of the graphene region. Figure 3F shows a layer-structured nanoparticle with a darker layer on top of a lighter layer, which may be interpreted as a layer of dense IO coated on top of a graphene surface. The inset of Figure 3G shows our proposed structure of MGQD, with IO coated on top of the folded graphene sheets and with some edges of graphene sheets uncovered due to the fracture of IO-graphene during the hydrothermal reduction. As the residual IO precursors and IO were removed from GO-IO nanoparticles before hydrothermal treatment, we expect the amount of individual A-IO particles present in the MGQDs to be minimal, if any.

As described previously, the average thickness of the MGQDs from AFM is 2.3 nm, which is thicker than the reported thickness of graphene (0.37 nm [46]), rGO (~0.8 nm [47]) or the GQDs prepared using the same hydrothermal reduction method (1.5 nm [40]). This suggests that the IO coating on both sides of the MGQD surface is likely 0.8 – 1.9 nm thick; however, we do not exclude the possibility of the presence of some residual thicker nanoparticles in the MGQD. IO growth on GO was reported to be smaller than pristine IO growth due to the dispersed nucleation of Fe^{3+} by the oxygen functional groups (C=O) of GO [48], and a similar effect may have occurred during the synthesis of the IO on the GO-IO followed by reduction of GO into rGO during hydrothermal cutting.
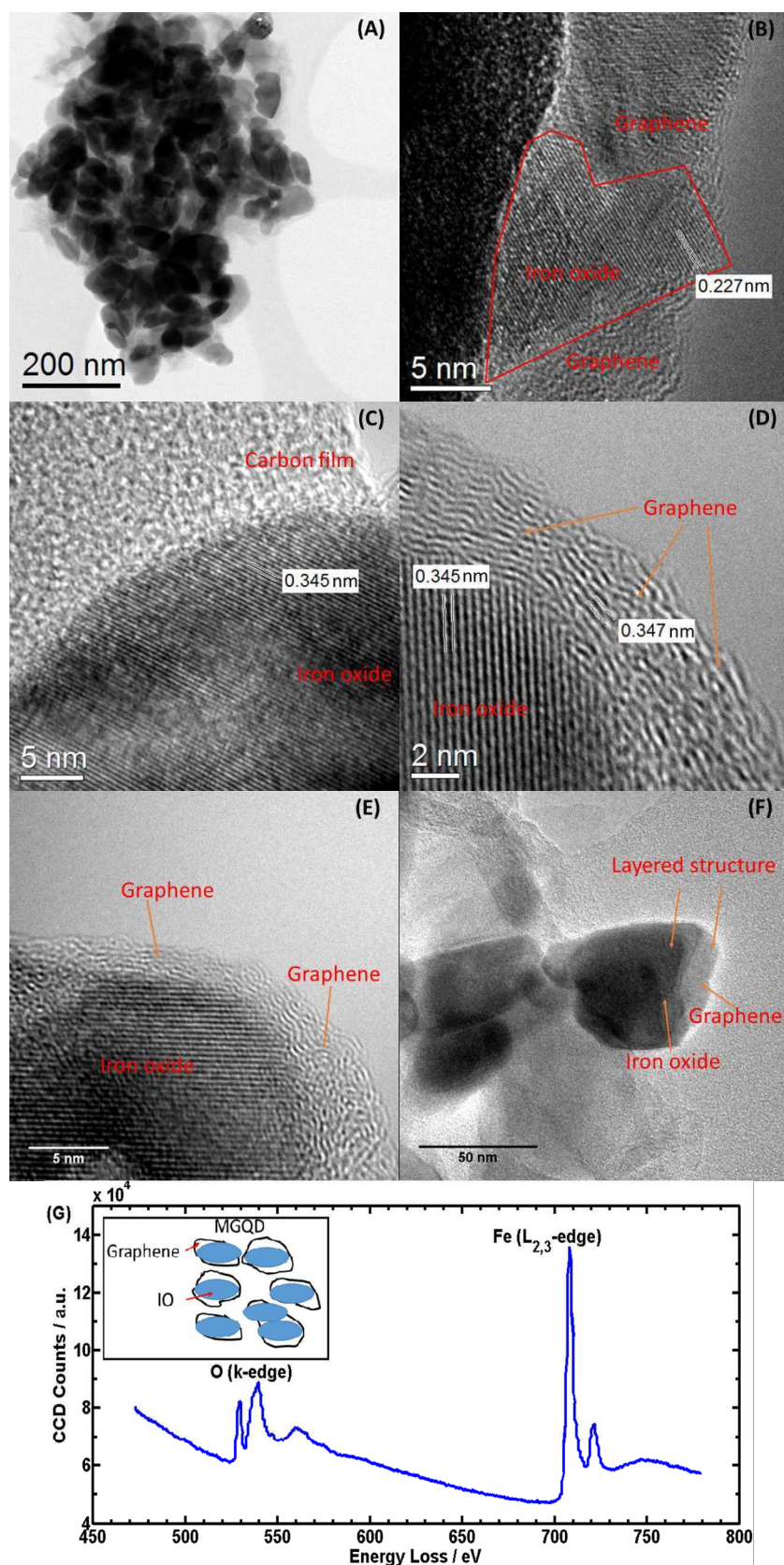
Figure 3 (A-F) HR-TEM images of MGQDs, showing (A) a cluster of MGQDs on amorphous carbon film support showing distinguishable individual MGQDs, (B) a region of IO on graphene (rGO), (C) a region of IO on carbon film support, (D-E) a region of IO on graphene, (F) an example of the layered structure of the MGQD, showing a graphene base with IO layer on top; (G) EELS spectrum of MGQDs, showing a composition of oxygen and iron, (Inset: Scheme of the proposed structure of the MGQDs).

12
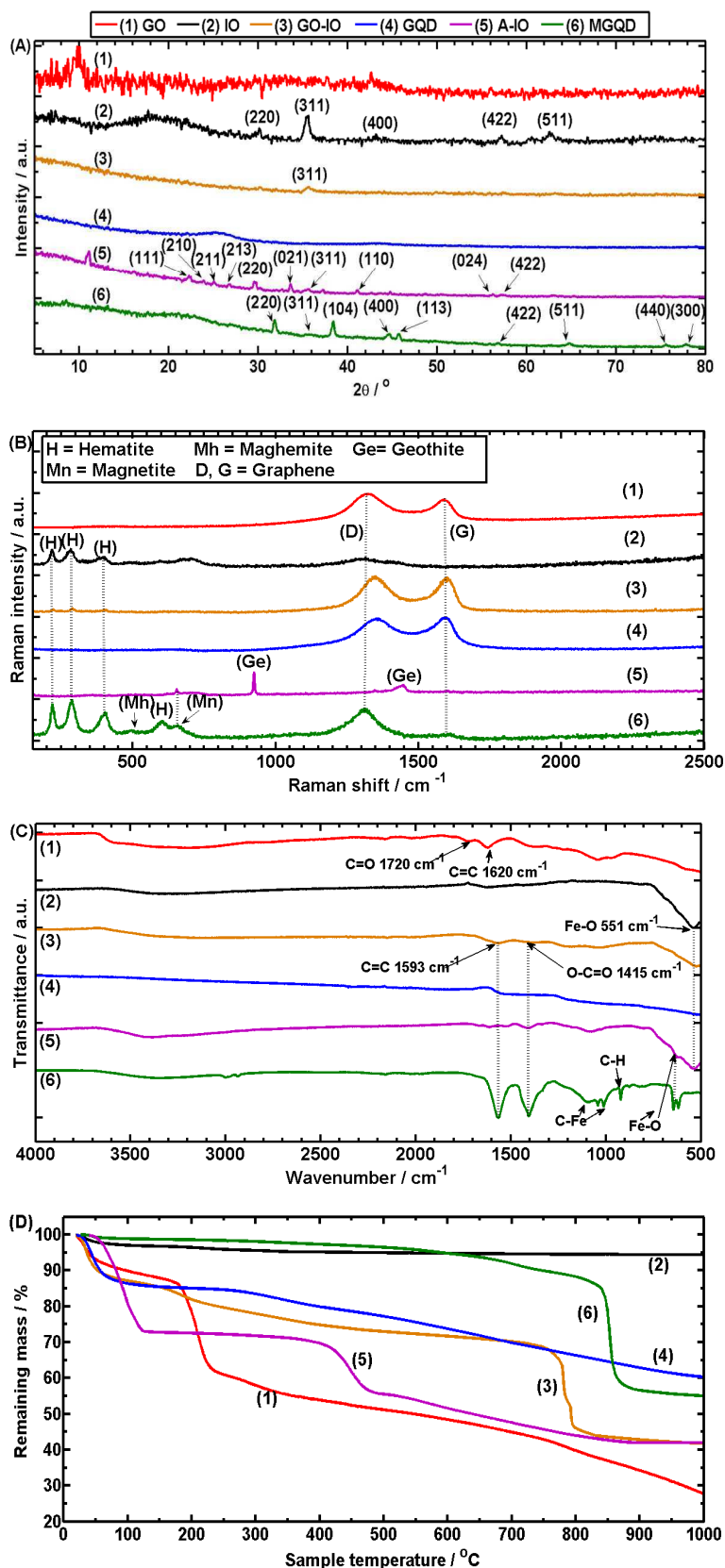
Figure 4 (A) XRD traces, (B) Raman spectra (C) FT-IR spectra and (D) TGA curves of GO, IO, GO-IO, GQDs, A-IO, and MGQDs.

The composition of the MGQD in Figure 2A-2 can be seen in the EDS spectrum in Figure 2C, which confirms the presence of iron (0.72, 6.42, and 7.08 keV) [49,50]. The oxygen (0.54 keV) was from the IO and the residual oxygenated groups in the

hydrothermally reduced GO while carbon (0.3 keV) was from the rGO and carbon-coated copper grids (0.94, 8.06, and 8.92 keV) [49,51]. The SAED pattern (Figure 2C, Inset) has the ring patterns associated with (220) and (104) diffraction peaks of magnetite and hematite (α-Fe_2O_3) respectively [52,53]. The EELS spectrum of a thin layer-structured nanoparticle acquired from HR-TEM (Figure 3G) confirms the presence of IO on the MGQD, as shown by the oxygen K-edge peaks at 529, 540, and 561 eV and the iron $L_{2,3}$ peaks at 708 and 722 eV [54].

The results from XRD (Figure 4A) confirm that the MGQDs are characterized by both rGO and a mixture of magnetite, maghemite (γ-Fe_2O_3), and hematite. GO has been oxidized from graphite and is largely exfoliated (weak (002) peak at $2\theta = 10.6^{\circ}$) [33]. IO is crystalline, with a (220) peak at $2\theta = 30.7^{\circ}$, a strong (311) peak at $2\theta = 35.5^{\circ}$, a (400) peak at $2\theta = 43.2^{\circ}$, a (422) peak at $2\theta = 57.2^{\circ}$, and a (511) peak at $2\theta = 62.5^{\circ}$ [53,55–57]. This corresponds with the JCPDS 19-0629 card for magnetite, as IO possesses the (311), (220), (511) and (422) peaks that are common to both magnetite and maghemite but lacks of the characteristic (210), (211) and (213) peaks of maghemite (JCPDS 39-1346) [53,58]. GO-IO displays a distinct (311) peak from the IO, with the other peaks at a lower intensity, showing that the magnetite is formed before the hydrothermal treatment, as previously reported [8]. GQDs are characteristic of rGO ((002) peak at $2\theta = 25.4^{\circ}$) [59]. A-IO is a mixture of magnetite, maghemite, and hematite (the α- mineral form of maghemite), with the (311), (220), and (422) peaks from the IO, maghemite specific peaks (210), (211), (213), and hematite characteristic peaks (021), (110), (024) (JCPDS 33-0664) indicated on the curve [53,60]. The presence of hematite is caused by the partial topotactic oxidation of magnetite at 200 $^{\circ}$C during autoclaving [61]. The MGQD curve shows a change in structure from both GQD and A-IO. rGO can be identified by the weak (002) peak at $2\theta = 21.6^{\circ}$. This peak has shifted by 3.8° when compared to the GQD curve, which may stem from the reaction of GO and IO during autoclaving that may have altered the crystalline structure (*vide infra*) [62]. The effect of rGO within the MGQDs has caused a reduction in intensity of the (311) and (511) peaks from IO, a new (440) peak at $2\theta = 76.0^{\circ}$ common to magnetite and maghemite, and the introduction of a (104) peak at $2\theta = 38.3^{\circ}$, a (113) peak at $2\theta = 45.5^{\circ}$, and a (300) peak at $2\theta = 78.1^{\circ}$, all from hematite [53].

A further analysis of the structure of the MGQDs and the structural change during autoclaving was performed through Raman spectroscopy of GO, IO, GO-IO, GQDs, A-IO and MGQDs (Figure 4B). GO can be identified by the G band at 1591 cm^{-1} (E_{2g} mode) and the D band at 1322 cm^{-1} (A_{1g}) [63]. The IO is a mixture of magnetite and maghemite, with the maghemite caused by the local extreme heating of the IO powder by the laser source as it was

14

not identified in the XRD analysis [64,65]. The peak at 300 cm^{-1} and the broad peak at 660 cm^{-1} are assigned to magnetite T_{2g} and A_{1g}, while the peaks at 217, 283 and 401 cm^{-1} are attributed to hematite $A_{1g}(1)$, $E_g(2 + 3)$, and $E_{2g}(4)$ [61,64,66]. The GO-IO spectrum is a combination of the characteristic peaks of the GO and IO spectra, again showing the successful seeding of IO crystals onto the GO nanosheets. The GQDs can be identified by the G band at 1594 cm^{-1} (E_{2g} mode) and the D band at 1359 cm^{-1} (a_{1g}), with the ratio of the intensities of the D peak to the G peak decreasing relative to GO, showing an increase in the sp^2 carbon structure of pristine graphene and graphite. A-IO is characterized as a mixture of magnetite and hematite, with a magnetite peak at 653 cm^{-1} [64,67] and a hematite peak at 619 cm^{-1} [53,64,67], and with additional goethite (α-FeOOH, the hydrated form of hematite) peaks at 924 cm^{-1} and at 1442 cm^{-1} [68]. MGQDs can be seen to be magnetite (656 cm^{-1}) [64,67], maghemite (broad peak at 500 cm^{-1}) [64,67], hematite (peaks at 218, 287, 402, and 604 cm^{-1}) and rGO (G peak at 1588 cm^{-1}) [63]. The Raman spectrum of the MGQDs is closer to GO-IO than to A-IO. Presumably this is because the IO within the MGQD is magnetite, like with GO-IO while the A-IO is mainly composed of maghemite and hematite. The IO of MGQD is in the form of a film on the surface of the MGQD as previously described, and only has one outer surface exposed to the effects of the hydrothermal treatment, unlike the A-IO particles which have all the surfaces exposed. This reduces the effect of the hydrothermal reaction on the IO on graphene surface, leading to a different chemical composition.

FT-IR spectra of the nanomaterials are shown in Figure 4C. GO has C-O bonds at 1043 cm^{-1}, C=C bonds at 1621 cm^{-1} and C=O bonds at 1720 cm^{-1}. On the IO spectrum, a peak for the Fe-O bond is present at 551 cm^{-1} [8]. For the GO-IO, the synthesis procedure of IO on the GO has led to the shift of the C=C aromatic bonds of the GO from 1621 cm^{-1} to 1593 cm^{-1} and to the creation of O-C=O bonds at 1415 cm^{-1} [69]. The Fe-O peak has been maintained and is at 527 cm^{-1}. The GQD curve shows a reduction in functional groups in comparison to GO, with the peaks barely visible on the curve, confirming the reduction of GO to rGO. A-IO possesses 622 and 537 cm^{-1} peaks attributed to Fe-O peaks [66]. MGQDs have 646, 619 and 462 cm^{-1} peaks attributed to Fe-O bonds from magnetite, maghemite and hematite, a C=C peak at 1564 cm^{-1} and O-C=O peak at 1406 cm^{-1} peak that are similar to GO-IO, and 1086 and 1012 cm^{-1} peaks attributed to C-Fe bonds confirming the chemical bonding between rGO and IO [66].

Figure 4D shows the TGA curves of the MGQD and its control samples in a nitrogen atmosphere. TGA suggests that GO is oxidized graphene (dissociation of epoxide and hydroxyl groups at ~200 ^{o}C is 23% of the total dry mass). IO has limited dissociation of ~5% (similar to magnetite) as it does not possess any functional groups on the surface to be

15

dissociated [70]. GO-IO is a mixture of GO and IO with a main mass loss (~27% of the dry mass) at ~780 ^{o}C, attributed to the reaction of IO with carbon from rGO to release CO and CO_2 gases [71]. The GQDs are rGO (reduced mass loss as compared to GO at ~200 ^{o}C, 0.5% of the total dry mass). A-IO has a major mass loss between 400 and 500 ^{o}C (~19% of the dry mass) that is attributable to the phase transformation from maghemite to hematite; this phase transformation may be accompanied by other transformations such as conversion of maghemite to an intermediate product magnetite [53,71–73]. The MGQDs have a minor mass loss step at ~720 ^{o}C (~3% of the dry mass), which could be due to the reaction between α-Fe_2O_3 and carbon of graphene [73], resulting in the release of CO and CO_2. The major mass loss at ~780 ^{o}C in the curve for GO-IO has moved to ~850 ^{o}C (with a loss of ~32% of the dry mass), which may be the result of autoclaving that has caused phase transformation of the IO and the chemical bonding between IO and rGO.

ICP-MS analysis calculated the quantity of Fe in the MGQD as 448 g kg^{-1}. Theoretically, the amount of Fe in Fe_2O_3 is 70.0 wt.% and in Fe_3O_4 is 72.4 wt.%. If the amount of Fe in the MGQDs is 447.89 g kg^{-1} (considering the measurement error as 0.11 g kg^{-1} measured for GQDs using the same process), this allows for the mass percentage of IO within the MGQDs to be calculated as between 62 – 64 wt.%, with the remainder being the rGO. This suggests that IO is the major component of the MGQDs with graphene as the minor component. The density of the MGQDs was measured through pycometry as 3.66 (± 0.006) g cm^{-3} for MGQDs. In comparison, the density of GQDs was 1.66 (± 0.006) g cm^{-3}, slightly higher than that for chitosan-reduced rGO (1.46 g cm^{-3}) [74] because of the absence of chitosan in the GQDs. The increase in density of the MGQDs over the value of GQDs is due to the higher density of the IO within the MGQD structure, e.g. 4.9 – 5.2 g cm^{-3} for magnetite [41].

### 3.2 Photoluminescent and magnetic properties

The photo-physical properties of the nanoparticles were characterized using steady-state UV-Vis spectroscopy. As shown in Figure 5A, MGQDs and GQDs have absorbance peaks at 270 nm and 320 nm, with the MGQDs also exhibiting the characteristic absorbance trait of A-IO in the wavelength region 400 to 500 nm. The emission characteristics of the MGQDs are presented in Figure 5B. Here, excitation of the MGQDs at 320 nm (corresponding to the peak in the excitation spectrum) yields an emission spectrum with a peak at 398 nm. This emission value is slightly lower than that (420 nm) observed for the GQDs prepared by the same hydrothermal method [40]. Quantum yield measurements (using Equation 1) gave a value of 7.9% for the MGQDs, similar to the published literature for GQDs (5.5-14%) prepared by

other groups [20,23,24,75] and slightly lower than the GQDs prepared using the same method (9.4%) [40]. These suggest the presence of IO slightly quenches the luminescence of GQDs. The photos in the inset confirm the photoluminescence (PL) properties of the MGQDs (right), in contrast to the control sample of PBS solution. MGQDs, in a 1 mg ml^{-1} aqueous suspension, have a PL lifetime of 1.9 ns (Figure 5C), similar to GQDs and conventional QDs in the literature (range of 1-10 ns) [76–79], and slightly lower than the GQDs prepared using the same method (2.3 ns) [40].
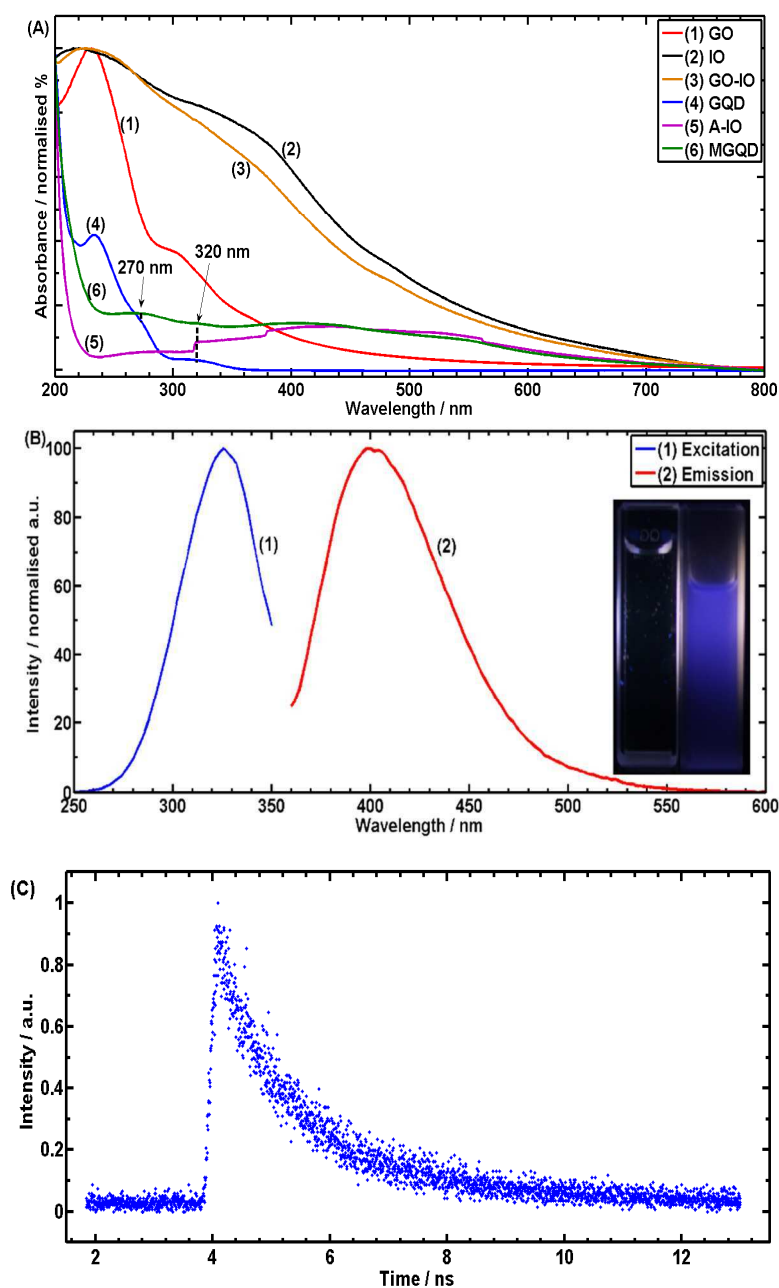
Figure 5 (A) UV-Vis spectra for GO, IO, GO-IO, GQDs, A-IO and MGQDs (0.3 mg ml^{-1} concentration in distilled water); (B) Photoluminescence spectra of MGQDs showing the excitation wavelengths versus emission wavelengths; (Inset) Photoluminescent imaging of (left) PBS and (right) MGQDs in PBS under 360 nm light; (C) PL lifetime data for MGQDs in an aqueous suspension (1 mg ml^{-1}).

Previously reported GQDs with attached IO (GQD-IOs) did not possess PL properties as they synthesized GQDs first and then attached IO [15]. Coating of IO onto the GQDs quenched the fluorescence of GQDs, which is similar to the quenching behavior of gold nanoparticles bonded to semiconductor QDs [80]. It was theorized that a QD would have its fluorescence quenched by a non-radiative energy dissipation process from the bonded nanoparticles, and not explicitly through a decrease in the radiative (PL) properties of the QD itself [80,81]. In our process the GO-IO was synthesized first and then reduced to MGQDs; the reduction procedure broke the GO-IO into small QDs (Figure 2), with the edges of the core-GQD within the MGQD now exposed. These edges have a zigzag structure that contain triple carbenes [82] which are linked to the electron orbital transition at 320 nm [25], and so the PL properties of GQDs are preserved.
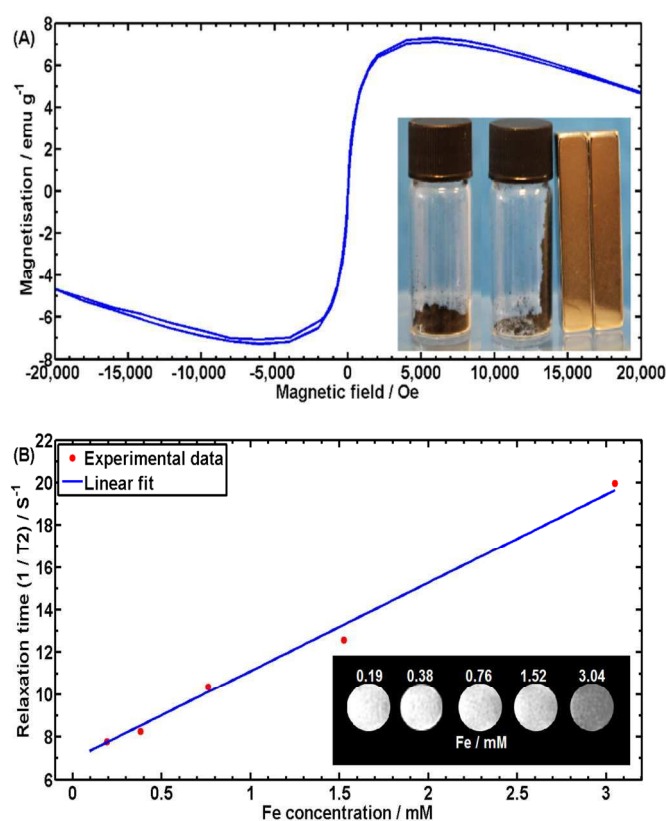
Figure 6 (A) Magnetic hysteresis loop of MGQDs and (Inset) digital images of the effect of external magnetic stimulation upon MGQD powder, (left) before and (right) after a magnet is placed beside it. (B) T2 relaxation time of MGQDs from M.R.I. and (Inset) digital images of MGQDs as contrast agents, as a function of increasing Fe concentration.

The magnetic hysteresis loop of MGQDs (Figure 6A), determined with a SQUID, illustrate that they possess no residual magnetization and are superparamagnetic. The saturation magnetization of the MGQDs was 7.31 emu g^{-1}, comparable to other magnetic nanoparticles (4.62 emu g^{-1}) [8]. As demonstrated in Figure 6A (Inset), the MGQDs can be drawn towards a magnet from a resting position. Figure 6B is the T2 relaxation time of

MGQDs from M.R.I., with the slope of the relaxation time determined as 4.16 mM^{-1} s^{-1}. In comparison, the slope of the relaxation time of magnetite can vary from 35.48 to 114 mM^{-1} s^{-1} [14,83], maghemite had a slope of 43.3 mM^{-1} S^{-1} [84], and gadolinium-doped graphene and a GO-IO-manganese oxide nanoparticle had slopes of 108 mM^{-1} s^{-1} [85], and 65.9 – 103 mM^{-1} s^{-1} [86], respectively. The relaxation time slopes of nanoparticles that contain IO vary due to the different Fe concentrations of the nanoparticles used [14,83,86]. Figure 6B (Inset) shows digital images of MGQDs as contrast agents as a function of increasing Fe concentration. The results of the PL and magnetic properties tests confirm that the MGQDs can potentially be used for dual-modality fluorescent and M.R.I. applications.

3.3 Cell viability and imaging

MGQDs were found to have limited cytotoxicity up to a concentration of 50 µg ml^{-1} in MTT cell viability tests (Figure 7A). Suspensions of MGQDs of 20 and 50 µg ml^{-1} in DMEM gave cell viability levels of 70 – 75% compared to cell culture on tissue culture plastic at an initial 6 h and 24 h incubation times, suggesting that they have a low cytotoxicity. The cell viability values for MGQDs are similar to those recorded for pristine IO nanoparticles used for M.R.I. (80% for 50 µg ml^{-1}) [87] and other GQDs reported before that are used for fluorescent imaging (70-80%) [20,24,26,27]. There is a dose dependent cytotoxic effect with a steep decrease in cell viability from 50 µg ml^{-1} to 500 µg ml^{-1}. The visual effects of acute exposure (6 h incubation) to MGQDs shown in Figures 7B-1 – 7B-6 for cells which were subsequently cultured for a further 72 h. Cells which had encountered 20 and 50 µg ml^{-1} MGQDs grew well showing no long term adverse effects while cells which were exposed to concentrations of 100, 200 and 500 µg ml^{-1} did not recover and increase in number over the 72 h (Figures 7B-4 – 7B-6). Many of these cells are seen as the compact, white, and circular nodes: an appearance that was previously reported to indicate apoptosis [88].

The cell viability of nanoparticles at higher concentrations can be improved upon by passivation with a coating of a biocompatible organic compound, with amine functionalized GQDs [23] and IO functionalized by pullulan [87] significantly improving the cell viability of the respective nanoparticles. Chitosan could also act as a passivation agent as previous work has shown that chitosan functionalized rGO was more stable in simulated body fluids than pristine GO [89], and that chitosan functionalized graphene nanosheets are biocompatible and do promote the proliferation of cells [90].
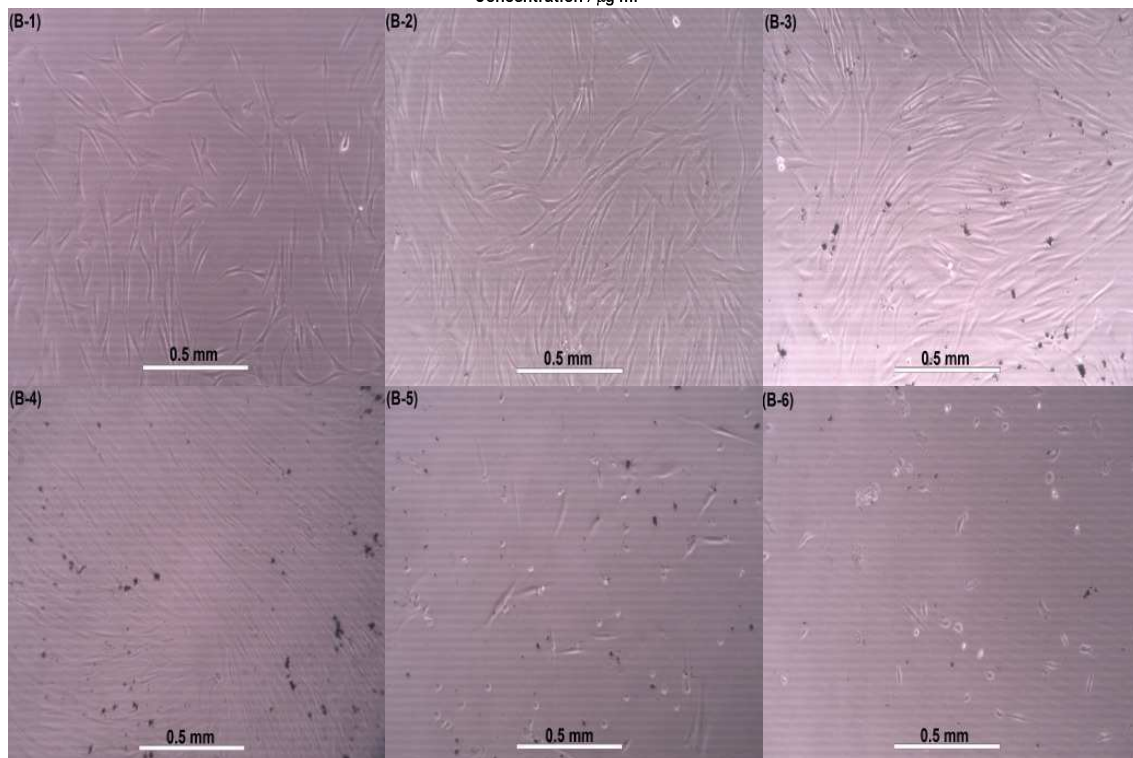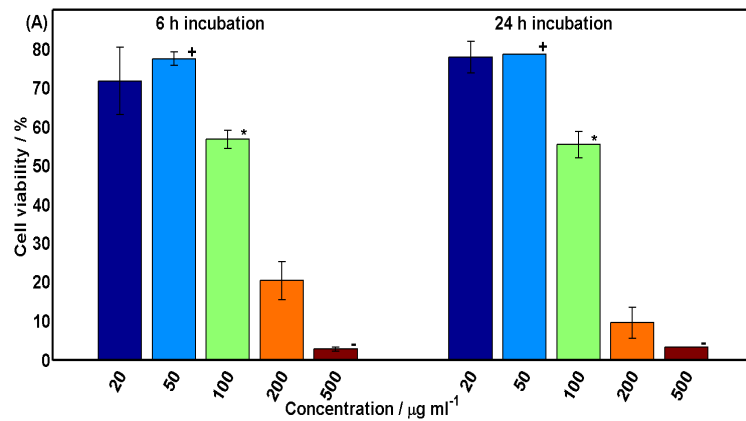
Figure 7 MTT cell viability results for MGQDs treated fibroblast cells. Concentrations used were 20, 50, 100, 200, and 500 µg ml^{-1} in DMEM medium and the initial incubation times were 6 h and 24 h. Cells were then washed and cultured for a further 72 h before viability was assessed. Bars with the same symbols (*, +, -) were statistically similar to each other (p < 0.05). Optical microscopy images of the cells were taken 72 h after an initial 6 h incubation with MGQDs. Concentrations used were (B-1) 0 (control), (B-2) 20, (B-3) 50, (B-4) 100, (B-5) 200, and (B-6) 500 µg ml^{-1}.
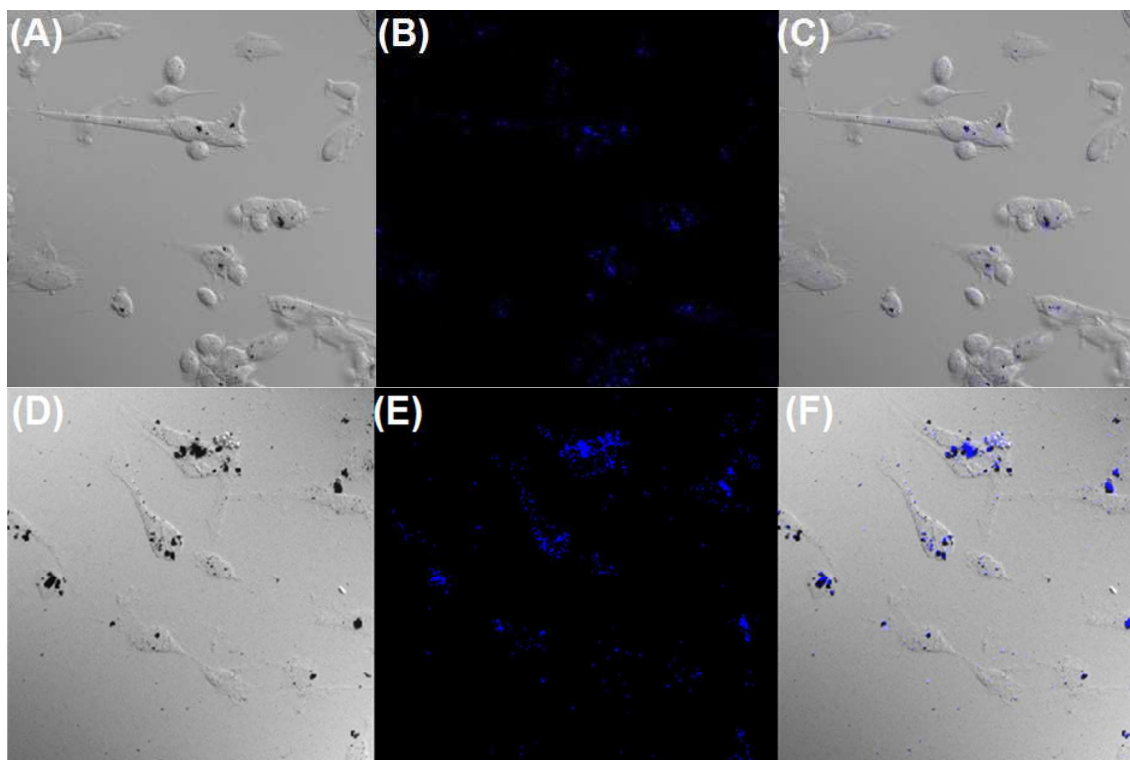
Figure 8 Optical microscopy images of fibroblast cells after an initial 12 h incubation with MGQDs. Concentrations used were (A-C) 50 µg ml^{-1} and (D-F) 100 µg ml^{-1}. (A) and (D) are the fibroblast cells under normal light, and (B) and (E) are under fluorescent light. (C) and (F) are an overlay of the white and fluorescent light images.

Figure 8 shows fibroblast cells under 345 nm irradiation that have been treated with (A-C) 50 µg ml^{-1} and (D-F) 100 µg ml^{-1} of MGQDs for 12 h. Figure 8 C and F are overlaid white light (Figure 8 A and D) and fluorescent light (Figure 8 B and E) images, showing that the emission of fluorescent light is from within the cells which suggests that the MGQDs entered the cells for both suspension concentrations. The emission is concentration dependent, with the emission from the cells stronger when treated with 100 µg ml^{-1} of MGQDs than with 50 µg ml^{-1}; the higher concentration of MGQDs in the suspension allowed for more MGQDs to be internalized into the cells, but higher concentrations have been shown to be cytotoxic after a long period of incubation (Figure 7A). Nevertheless, at 50 µg ml^{-1} it is still possible to image the nanoparticles. When surface-treated with a passivation agent, MGQDs at a higher concentration such as 100 µg ml^{-1} may also be used without incurring toxicity to cells.

3.4 Drug delivery

The physical bonding of the anesthetic lidocaine hydrochloride (LH) (Figure 9A, inset) onto MGQDs to form MGQD-LH is mainly through π-π stacking between the aromatic rings of the MGQDs and LH [91]. Figure S2 shows the transposing of LH peaks onto MGQD in FT-IR (S2A) and Raman (S2B) spectra, showing that the LH is adsorbed to the surface of the

MGQDs. A comparison of TGA curves of MGQD-LH with LH and MGQD (Figure 9A) allows for the quantity of the drug in MGQD-LH to be estimated as 24 wt.%, giving an estimated loading ratio of LH:MGQD of 0.31:1. The drug release profile (Figure 9B) determined that the release of LH from MGQD-LH into the PBS achieved ~100% (106.9 ± 13.1%) of the total drug available, or 5.09 (± 0.63) mg ml^{-1}, at 8 h, after which the test was terminated.
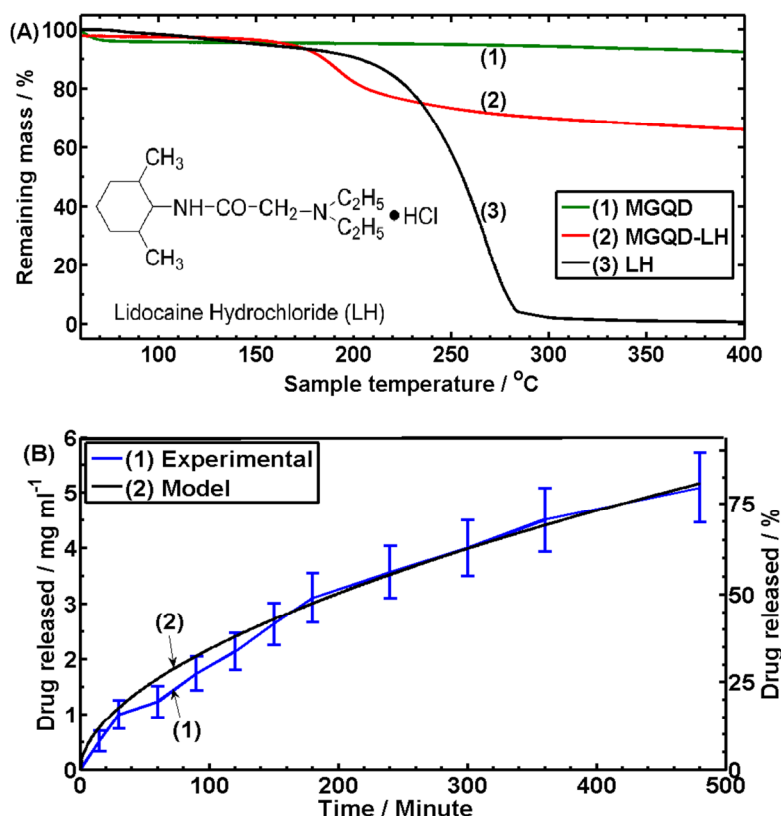
Figure 9 (A) TGA curves for MGQD, MGQD-LH and LH (Inset: chemical structure of LH). (B) The release of LH from MGQD-LH over the course of 8 h.

To determine if the diffusion of LH from the MGQD follows Fickian law, Equation 2 was used [92]:

$$\frac{Q_t}{Q_T} = K \times t^n \tag{2}$$

in which Q_t is the amount of drug released at the time "t", Q_T is the total amount of drug released during the experiment, K is the diffusion coefficient and n is the diffusion release exponent. It was found that the values of 0.56 µg s^{-1} and 0.55 for K and n best fit the experimental data presented in Figure 9B. This shows that the diffusion of the LH from the MGQD was not Fickian but anomalous [93] at pH = 7.4, similar to the diffusion of doxorubicin from GO [94] and rhodamine B from GO into a solution of pH = 4.5 [95]. These results indicate that a drug can be bonded to the surface of MGQDs and then be gradually released from the MGQDs into the body. It has been previously shown in the literature that

22

similar nanoparticles like carbon QDs [28], GO [96] and IO [6] can be extracted from the blood and collect in the spleen/bladder to be excreted from the body through urine.

3.5 Photothermal properties
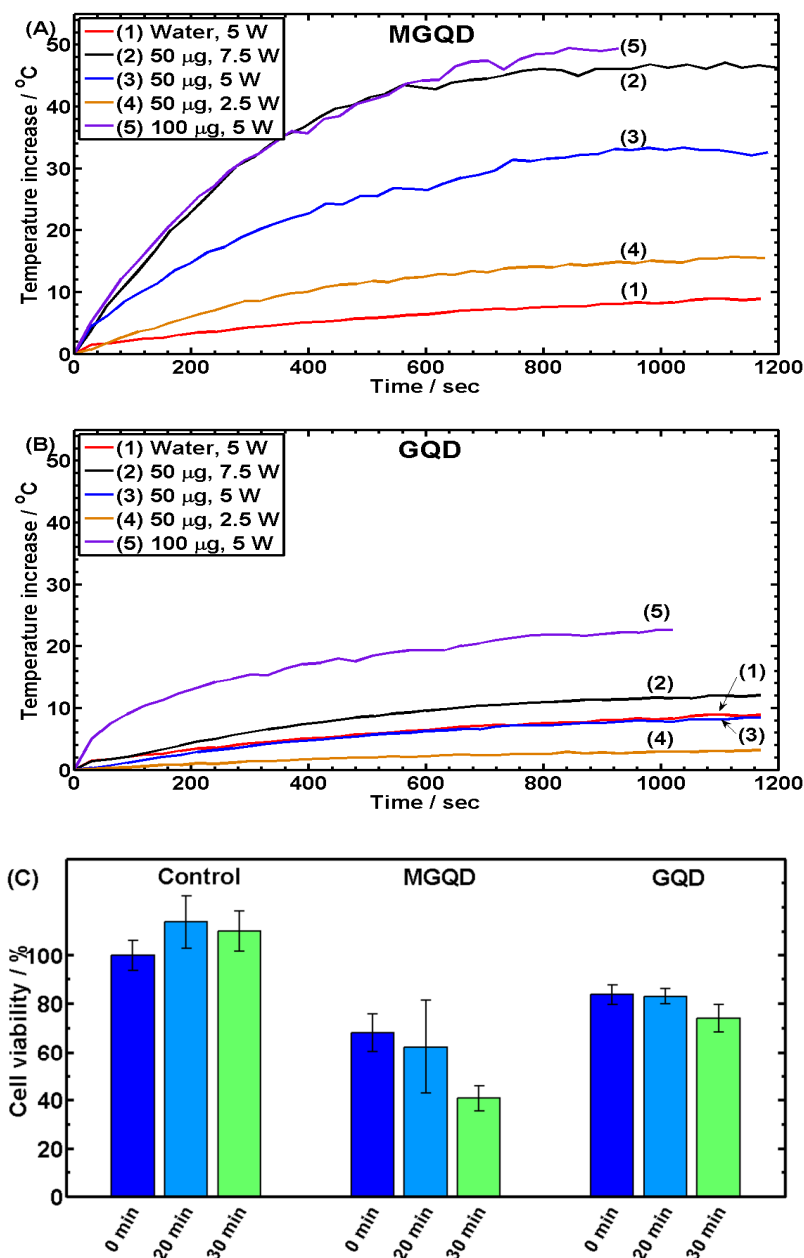
Figure 10 Temperature increase differential between (A) MGQD suspensions and (B) GQD suspensions, and distilled water (control) under NIR 808 nm laser irradiation with varying power. (C) CCK-8 cell viability of HeLa cells incubated with 50 µg ml^{-1} MGQD or GQD suspensions and irradiated with a 2.5 W cm^{-2} NIR laser (wavelength: 808 nm) for 0 min, 20 min, or 30 min. Control cells were pristine HeLa cells without QD treatment.

There is a possibility of using the MGQDs for cancer photothermal therapy, where the MGQDs absorb NIR light and convert it to heat that can be used to kill cancer cells locally [97]. To assess their potential for this application, suspensions of MGQDs in distilled water, together with GQD suspensions and distilled water control sample, were irradiated with a 2,

23

5, and 7.5 W cm^{-2} NIR laser (wavelength: 808 nm) for a period of time. The results (Figure 10) show that the temperature of the QD suspension increases with increasing laser power as well as QD concentration. After 20 min under 5 W cm^{-2} irradiation power, it can be seen that the temperature of the 50 µg ml^{-1} MGQD suspension increases by 32.6 °C, compared to 8.9 °C for the water control sample and 8.4 °C for the 50 µg ml^{-1} GQD suspension. This can be attributed to the higher absorption of the MGQDs in the NIR range (700-800 nm, Figure 5A) than the GQDs; this higher absorption is due to the presence of IO on the MGQDs. After 20 min, the suspension of 50 µg ml^{-1} MGQDs at 7.5 W cm^{-2} achieved a temperature increase of 46.3 °C; this is comparable to the increase of the 100 µg ml^{-1}MGQD suspension (49.4 °C) after 16 min at 5 W cm^{-2} irradiation. This concentration and laser power dependent result shows that the MGQDs can be used as an effective photothermal ablation agent at a low concentration that was determined to have low cytotoxicity (Figure 7). The differences in suspension concentration, irradiation time, and irradiation power make direct comparisons between previously reported photothermal therapy agents difficult. But, generally MGQDs compare well to other nanoparticles that are structurally and elementally similar, in particular GO-poly(ethylene glycol) (PEG) [13], rGO-PEG [13], GO-IO [9], and IO [14]. MQGDs also compare well to other photothermal agents such as carbon nanotubes [98] and gold nanoparticles [99].

The photothermal therapy results suggest that the MGQDs could be potentially used for the ablation of tumours, where the presence of MGQDs within the tumour will raise the temperature and kill tumour cells locally [97]. MGQDs and GQDs were incubated for 4 h with HeLa cells for *in vitro* photothermal ablation studies (Figure 10C). Under 2.5 W cm^{-2} NIR laser irradiation, untreated HeLa cells can be seen to have a similar cell viability, with statistical insignificance, to the untreated, non-irradiated cells. This shows that laser irradiation alone at this power density will not reduce the viability of the HeLa cells. The presence of MGQDs, without irradiation, reduced the cell viability of HeLa cells to 68%, compared to 84% for GQDs. These two values are lower than the values for fibroblast cells (Figure 7A) due to the different types of cell and incubation conditions used. There are two possible causes of this cell-specific susceptibility. MGQDs could have a higher cytotoxic effect on HeLa cells than on dermal fibroblast cells because of a higher susceptibility of HeLa cells to reactive oxide species than for the fibroblast cells, similar to the differing cell viability results for IO when incubated with mesothelioma cells and mice fibroblast that was attributed to reactive oxide species damage [100]. This difference may be due also to the rate of uptake of the MGQDs into the differing cells [100]; for example, a previous report [101] shows the differing rates of uptake for uncoated IO into mouse macrophage and human breast

cancer cells. Coating the IO with a biocompatible polymer such as PEG can lower the reactive oxide species effect on cells and affect the rate of uptake into cells [101], which may increase the cell viability of HeLa cells treated with MGQDs if desired. There is a time dependent decrease in cell viability, with a more substantial decrease in cell viability occurring when the HeLa cells that were treated with MGQDs were irradiated for 30 min than for 20 min (cell viability of 41% versus 62%, respectively). GQDs, under irradiation, did not reduce the cell viability of the HeLa cells by as much, achieving a reduction to 83% and 74% for 20 min and 30 min irradiation time, respectively. This difference between the GQDs and the MGQDs is in accordance with the temperature increases from the photothermal measurement.

Previously, QDs such as CuS [102,103] were used as photothermal ablation agents under irradiation with a 808 nm laser, with the QDs reducing the viability of HeLa cells [102] and of U87 glioblastoma cells [103]. When irradiated for 5 min with a 12 W cm^{-2} NIR laser, around ~65% of the tumour tissue in mice treated with CuS QDs showed signs of necrosis [103]. rGO-IO nanosheets achieved the full ablation of 4T1 tumours in mice that were treated with a 5 min exposure of 0.5 W cm^{-2} near-infrared laser irradiation [12]. In comparison to these results, our MGQDs are not as efficient as photothermal ablation agents under the laser irradiation conditions that we use, but they do offer bimodal imaging, with intrinsic M.R.I and fluorescent imaging capability. Also by increasing the laser power density (but still within the safe-use range), the photothermal ablation effect of the MGQDs may be improved.

3.5 Biostability

The stability of the MGQDs in biological fluids, including water, PBS and FCS, was assessed and the results are shown in Figure 11. It can be seen that pristine MGQDs partially aggregate in distilled water and PBS (pH = 7.4) within 2 h, with larger particles falling to the bottom of the container, but the remaining particles remained stable in suspension as the quantity of aggregates did not increase with time up to 24 h. The IO on the surface of MGQD is hydrophobic [104] and aggregates in water and in PBS. MGQDs in FCS aggregated significantly within 2 h, presumably due to the crosslinking of MGQDs by hydrogen bonding of the proteins in the FCS with the remaining –COOH groups on MGQD edges [105]. The coating of LH onto the MGQD surface has reduced this crosslinking effect and greatly improved the biostability of the MGQD over 10 days (Figure 11E), with minimal further aggregation of the MGQD-LH after the initial 2 h. In solution, LH maintains a positive ionic charge [106], and in FCS the LH coating prevents the MGQDs from aggregating through electrostatic repulsion. Coating the MGQDs with another ionic biopolymer, such as chitosan,

may also improve the stability of the MGQDs, similar to the improvement afforded to chitosan-coated rGO [89], as well as decreasing the cytotoxicity of the MGQDs [90].
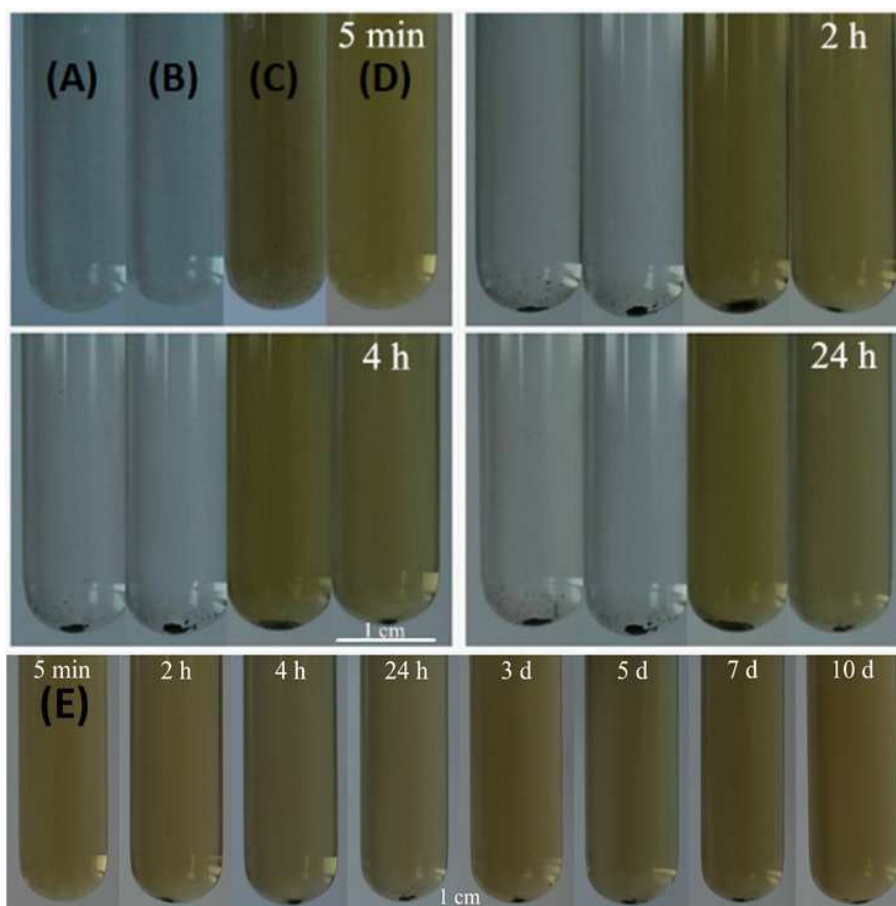
Figure 11 The biostability of (A-C) MGQDs and (D) MGQD-LH suspensions in solutions of (A) distilled water, (B) PBS (pH=7.4), (C-D) FCS. (E) MGQD-LH biostability in FCS over 10 days, showing that the drug coated MGQD is relatively stable in biological fluid over the test period of time.

4. Conclusions

The synthesis of MGQDs through the hydrothermal reduction of a water suspension of GO-IO nanoparticles was shown. The MGQDs were found to be around 45 nm in diameter and 2.3 nm high from TEM and AFM, with a composition of carbon, oxygen, and iron identified from EDS and EELS. Iron oxide was coated onto the graphene surface as a thin film and maybe also as individual particles within the bulk MGQDs. A mixture of iron oxides (magnetite, maghemite, and hematite) and rGO was formed during the hydrothermal reduction process, as determined from XRD, Raman spectroscopy, FT-IR and TGA. MGQDs emitted violet light with a wavelength of 398 nm when excited at 320 nm, showing excellent photoluminescent properties. They were also superparamagnetic, as determined by magnetic hysteresis analysis, and could act as a T2 contrast agent in M.R.I. applications.

A safe dosage level of 50 µg ml^{-1} was determined through cell viability testing with dermal fibroblasts for 24 h. Cells which had encountered a concentration of 50 µg ml^{-1} or lower of MGQDs grew well and showed no long term adverse effects. The MGQDs (50 µg ml^{-1} or 100 µg ml^{-1}) entered the cells after incubation for 12 h and could be detected by fluorescent imaging. A model drug was successfully bonded to the MGQDs, with a loading ratio of 0.31:1 (LH:MGQD), as characterized by FT-IR, Raman spectroscopy and TGA. The full release of the drug from the MGQD surface was achieved within 8 h. MGQDs, under NIR irradiation, generated a higher temperature than GQDs or distilled water due to the presence of iron oxide which is a more effective NIR absorber, and could achieve more significant temperature increases at a low concentration and laser power. This higher NIR absorption allowed for the MGQDs to reduce the cell viability of cancer cells during *in vitro* laser ablation experiments by a greater amount than was possible with GQDs. Ionic drug coated MGQDs were shown to have a better stability in FCS than uncoated MGQDs, which showed the coated MGQDs were relatively stable in FCS over the test period (10 days).

These results demonstrate that the MGQDs have a low cytotoxicity and they retained the photoluminescent properties of GQDs which, in conjunction with the superparamagnetic properties from IO nanoparticles, would allow for fluorescent and M.R.I. dual-modality imaging in biomedical applications without the need to use an additional fluorescent dye. Meanwhile, the MGQDs could be used as a targeted drug carrier via the physical bonding of a therapeutic to the MGQDs and the subsequent release of the therapeutic at the desired site by external magnetic stimulation, and as an effective potential agent for cancer photothermal therapy.

Acknowledgements

References

[1]   Feng L, Liu Z. Graphene in biomedicine : opportunities and challenges. Nanomedicine 2011;6:317–24.

[2]   Zhang Y, Nayak TR, Hong H, Cai W. Graphene: a versatile nanoplatform for biomedical applications. Nanoscale 2012;4:3833–42.

[3]   Goenka S, Sant V, Sant S. Graphene-based nanomaterials for drug delivery and tissue engineering. J Control Release 2014;173:75–88.

[4]   Figuerola A, Di Corato R, Manna L, Pellegrino T. From iron oxide nanoparticles towards advanced iron-based inorganic materials designed for biomedical applications. Pharmacol Res 2010;62:126–43.

[5]   Alexiou C, Jurgons R, Schmid R, Hilpert a, Bergemann C, Parak F, et al. In vitro and in vivo investigations of targeted chemotherapy with magnetic nanoparticles. J Magn Magn Mater 2005;293:389–93.

[6]   Weissleder R, Bogdanov A, Neuwelt EA, Papisov M. Long-circulating iron oxides for MR imaging. Adv Drug Deliv Rev 1995;16:321–34.

[7]   Bae KH, Park M, Do MJ, Lee N, Ryu JH, Kim GW, et al. Chitosan Oligosaccharide-Stabilized Ferrimagnetic Iron Oxide Nanocubes for Magnetically Modulated Cancer Hyperthermia. ACS Nano 2012;26:5266–73.

[8]   Yang X, Zhang X, Ma Y, Huang Y, Wang Y, Chen Y. Superparamagnetic graphene oxide–Fe3O4 nanoparticles hybrid for controlled targeted drug carriers. J Mater Chem 2009;19:2710–4.

[9]   Ma X, Tao H, Yang K, Feng L, Cheng L, Shi X, et al. A functionalized graphene oxide-iron oxide nanocomposite for magnetically targeted drug delivery, photothermal therapy, and magnetic resonance imaging. Nano Res 2012;5:199–212.

[10]   Shi X, Gong H, Li Y, Wang C, Cheng L, Liu Z. Graphene-based magnetic plasmonic nanocomposite for dual bioimaging and photothermal therapy. Biomaterials 2013;34:4786–93.

[11]   Ren L, Huang S, Fan W, Liu T. One-step preparation of hierarchical superparamagnetic iron oxide/graphene composites via hydrothermal method. Appl Surf Sci 2011;258:1132–8.

[12]   Yang K, Hu L, Ma X, Ye S, Cheng L, Shi X, et al. Multimodal imaging guided photothermal therapy using functionalized graphene nanosheets anchored with magnetic nanoparticles. Adv Mater 2012;24:1868–72.

[13]   Robinson JT, Tabakman SM, Liang Y, Wang H, Casalongue HS, Vinh D, et al. Ultrasmall reduced graphene oxide with high near-infrared absorbance for photothermal therapy. J Am Chem Soc 2011;133:6825–31.

[14]   Lin L-S, Cong Z-X, Cao J-B, Ke K-M, Peng Q-L, Gao J, et al. Multifunctional Fe3O4-polydopamine core-shell nanocomposites for intracellular mRNA detection and imaging-guided photothermal therapy. ACS Nano 2014;8:3876–83.

[15]   Wu X, Zhang Y, Han T, Wu H, Guo S, Zhang J. Composite of graphene quantum dots and Fe3O4 nanoparticles: peroxidase activity and application in phenolic compound removal. RSC Adv 2014;4:3299–305.

[16]   Zhu X, Wu W, Liu Z, Li L, Hu J, Dai H, et al. A reduced graphene oxide–nanoporous magnetic oxide iron hybrid as an improved anode material for lithium ion batteries. Electrochim Acta 2013;95:24–8.

[17]   Reed M, Randall J, Aggarwal R, Matyi R, Moore T, Wetsel A. Observation of discrete electronic states in a zero-dimensional semiconductor nanostructure. Phys Rev Lett 1988;60:535–7.

[18]   Derfus AM, Chan WCW, Bhatia SN. Probing the Cytotoxicity of Semiconductor Quantum Dots. Nano Lett 2004;4:11–8.

[19]   Guo G, Liu W, Liang J, He Z, Xu H, Yang X. Probing the cytotoxicity of CdSe quantum dots with surface modification. Mater Lett 2007;61:1641–4.

[20]   Bhunia SK, Saha A, Maity AR, Ray SC, Jana NR. Carbon nanoparticle-based fluorescent bioimaging probes. Sci Rep 2013;3:1–7.

[21]   Zhang X, Wang S, Zhu C, Liu M, Ji Y, Feng L, et al. Carbon-dots derived from nanodiamond: photoluminescence tunable nanoparticles for cell imaging. J Colloid Interface Sci 2013;397:39–44.

[22]   Zhuo S, Shao M, Lee S-T. Upconversion and downconversion fluorescent graphene quantum dots: ultrasonic preparation and photocatalysis. ACS Nano 2012;6:1059–64.

[23]   Jiang F, Chen D, Li R, Wang Y, Zhang G, Li S, et al. Eco-friendly synthesis of size-controllable amine-functionalized graphene quantum dots with antimycoplasma properties. Nanoscale 2013;5:1137–42.

[24]   Sun H, Wu L, Gao N, Ren J, Qu X. Improvement of photoluminescence of graphene quantum dots with a biocompatible photochemical reduction pathway and its bioimaging application. ACS Appl Mater Interf 2013;5:1174–9.

[25]   Pan D, Zhang J, Li Z, Wu M. Hydrothermal route for cutting graphene sheets into blue-luminescent graphene quantum dots. Adv Mater 2010;22:734–8.

[26]   Zhang M, Bai L, Shang W, Xie W, Ma H, Fu Y, et al. Facile synthesis of water-soluble, highly fluorescent graphene quantum dots as a robust biological label for stem cells. J Mater Chem 2012;22:7461–7.

[27]   Nurunnabi M, Khatun Z, Huh KM, Park SY, Lee DY, Cho KJ, et al. In vivo biodistribution and toxicology of carboxylated graphene quantum dots. ACS Nano 2013;7:6858–67.

[28]   Huang X, Zhang F, Zhu L, Choi KY, Guo N, Guo J, et al. Effect of injection routes on the biodistribution, clearance, and tumor uptake of carbon dots. ACS Nano 2013;7:5684–93.

[29]   Yong K-T. Mn-doped near-infrared quantum dots as multimodal targeted probes for pancreatic cancer imaging. Nanotechnology 2009;20:15102–12.

[30]   Singh N, Charan S, Sanjiv K, Huang S-H, Hsiao Y-C, Kuo C-W, et al. Synthesis of tunable and multifunctional Ni-doped near-infrared QDs for cancer cell targeting and cellular sorting. Bioconjug Chem 2012;23:421–30.

[31]   Yang H, Santra S, Walter GA, Holloway PH. GdIII-Functionalized Fluorescent Quantum Dots as Multimodal Imaging Probes. Adv Mater 2006;18:2890–4.

[32]   Selvan ST, Patra PK, Ang CY, Ying JY. Synthesis of silica-coated semiconductor and magnetic quantum dots and their use in the imaging of live cells. Angew Chem Int Ed Engl 2007;46:2448–52.

[33]   Marcano DC, Kosynkin D V, Berlin JM, Sinitskii A, Sun Z, Slesarev A, et al. Improved synthesis of graphene oxide. ACS Nano 2010;4:4806–14.

[34]   Kim EH, Ahn Y, Lee HS. Biomedical applications of superparamagnetic iron oxide nanoparticles encapsulated within chitosan. J Alloys Compd 2007;434-435:633–6.

[35]   Williams ATR, Winfield SA, Miller JN. Relative fluorescence quantum yields using a computer-controlled luminescence spectrometer. Analyst 1983;108:1067–71.

[36]   Blackwood KA, McKean R, Canton I, Freeman CO, Franklin KL, Cole D, et al. Development of biodegradable electrospun scaffolds for dermal replacement. Biomaterials 2008;29:3091–104.

[37]   Filipe V, Hawe A, Jiskoot W. Critical evaluation of Nanoparticle Tracking Analysis (NTA) by NanoSight for the measurement of nanoparticles and protein aggregates. Pharm Res 2010;27:796–810.

[38]   Shen J, Zhu Y, Yang X, Zong J, Zhang J, Li C. One-pot hydrothermal synthesis of graphenequantum dots surface-passivated by polyethylene glycol and their photoelectric conversion under near-infrared light. New J Chem 2012;36:97–101.

[39] Li Y, Zhao Y, Cheng H, Hu Y, Shi G, Dai L, et al. Nitrogen-Doped Graphene Quantum Dots with Oxygen-Rich Functional Groups. J Am Chem Soc 2011;134:15–8.

[40] Justin R, Román S, DX Chen, K Tao, Geng X, Grant RT, MacNeil S, K Sun, MacNeil S, Chen B. Biodegradable and conductive chitosan – graphene quantum dot nanocomposite microneedles for monitored delivery of both small and large molecular weight therapeutics. RSC Adv 2015, 5, 51934–51946.

[41] Li X, Yang H, Fu W, Wu C, Liu S, Zhu H, et al. Preparation of low-density superparamagnetic microspheres by coating glass microballoons with magnetite nanoparticles. Mater Sci Eng B 2006;135:38–43.

[42] Iida H, Takayanagi K, Nakanishi T, Osaka T. Synthesis of Fe3O4 nanoparticles with various sizes and magnetic properties by controlled hydrolysis. J Colloid Interface Sci 2007;314:274–80.

[43] Xie G, Xi P, Liu H, Chen F, Huang L, Shi Y, et al. A facile chemical method to produce superparamagnetic graphene oxide–Fe 3 O 4 hybrid composite and its application in the removal of dyes from aqueous solution. J Mater Chem 2012;22:1033–9.

[44] Wang G, Shen X, Yao J, Park J. Graphene nanosheets for enhanced lithium storage in lithium ion batteries. Carbon 2009;47:2049–53.

[45] Rümmeli MH, Kramberger C, Grüneis A, Ayala P, Gemming T, Büchner B, et al. On the Graphitization Nature of Oxides for the Formation of Carbon Nanostructures. Chem Mater 2007;19:4105–7.

[46] Koh YK, Bae M-H, Cahill DG, Pop E. Reliably counting atomic planes of few-layer graphene (n > 4). ACS Nano 2011;5:269–74.

[47] Zhang J, Yang H, Shen G, Cheng P, Zhang J, Guo S. Reduction of graphene oxide via L-ascorbic acid. Chem Comm 2010;46:1112–4.

[48] Qu Q, Yang S, Feng X. 2D sandwich-like sheets of iron oxide grown on graphene as high energy anode material for supercapacitors. Adv Mater 2011;23:5574–80.

[49] Chandra V, Park J, Chun Y, Lee JW, Hwang I-C, Kim KS. Water-dispersible magnetite-reduced graphene oxide composites for arsenic removal. ACS Nano 2010;4:3979–86.

[50] Carta D, Corrias A, Falqui A, Brescia R, Fantechi E, Pineider F, et al. EDS, HRTEM/STEM, and X-ray absorption spectroscopy studies of co-substituted maghemite nanoparticles. J Phys Chem C 2013;117:9496–506.

[51] Ji J, Zhang G, Chen H, Wang S, Zhang G, Zhang F, et al. Sulfonated graphene as water-tolerant solid acid catalyst. Chem Sci 2011;2:484–7.

[52] Bharde A, Rautaray D, Bansal V, Ahmad A, Sarkar I, Yusuf SM, et al. Extracellular biosynthesis of magnetite using fungi. Small 2006;2:135–41.

[53] Cornell RM, Schwertmann U. The Iron Oxides. Weinheim: Wiley - VCH; 1996.

[54] Zhang W, Stolojan V, Silva SRP, Wu CW. Raman, EELS and XPS studies of maghemite decorated multi-walled carbon nanotubes. Spectrochim Acta Part A Mol Biomol Spectrosc 2014;121:715–8.

[55] Tung TT, Feller J-F, Kim T, Kim H, Yang WS, Suh KS. Electromagnetic properties of Fe3O4-functionalized graphene and its composites with a conducting polymer. J Polym Sci Part A Polym Chem 2012;50:927–35.

[56] He F, Lam K, Ma D, Fan J, Chan LH, Zhang L. Fabrication of graphene nanosheet (GNS)–Fe3O4 hybrids and GNS–Fe3O4/syndiotactic polystyrene composites with high dielectric permittivity. Carbon N Y 2013;58:175–84.

[57] Sun Y, Ma M, Zhang Y, Gu N. Synthesis of nanometer-size maghemite particles from magnetite. Colloids Surfaces A Physicochem Eng Asp 2004;245:15–9.

[58] Kim W, Suh C-Y, Cho S-W, Roh K-M, Kwon H, Song K, et al. A new method for the identification and quantification of magnetite-maghemite mixture using conventional X-ray diffraction technique. Talanta 2012;94:348–52.

[59]   Wang X, Bai H, Yao Z, Liu A, Shi G. Electrically conductive and mechanically strong biomimetic chitosan/reduced graphene oxide composite films. J Mater Chem 2010;20:9032–6.

[60]   Jia C-J, Sun L-D, Yan Z-G, You L-P, Luo F, Han X-D, et al. Single-Crystalline Iron Oxide Nanotubes. Angew Chemie 2005;117:4402–7.

[61]   Pinna N, Grancharov S, Beato P, Bonville P, Antonietti M, Niederberger M. Magnetite Nanocrystals: Nonaqueous Synthesis, Characterization, and Solubility. Chem Mater 2005;17:3044–9.

[62]   Wang G, Chen G, Wei Z, Dong X, Qi M. Multifunctional Fe3O4/graphene oxide nanocomposites for magnetic resonance imaging and drug delivery. Mater Chem Phys 2013;141:997–1004.

[63]   Liu K, Zhang J-J, Cheng F-F, Zheng T-T, Wang C, Zhu J-J. Green and facile synthesis of highly biocompatible graphene nanosheets and its application for cellular imaging and drug delivery. J Mater Chem 2011;21:12034–40.

[64]   Shebanova ON, Lazor P. Raman spectroscopic study of magnetite (FeFe2O4): a new assignment for the vibrational spectrum. J Solid State Chem 2003;174:424–30.

[65]   Beattie IR, Gilson TR. The single crystal Raman Spectra of Nearly Opaque Materials: Iron (III) oxide and Chromium (III) oxide. J Am Chem Soc 1970:980–6.

[66]   Ramalakshmi M, Shakkthivel P, Sundrarajan M, Chen SM. Novel method of room temperature ionic liquid assisted Fe3O4 nanocubes and nanoflakes synthesis. Mater Res Bull 2013;48:2758–65.

[67]   Li Y-S, Church JS, Woodhead AL. Infrared and Raman spectroscopic studies on iron oxide magnetic nano-particles and their surface modifications. J Magn Magn Mater 2012;324:1543–50.

[68]   Chemelewski WD, Lee H-C, Lin J-F, Bard AJ, Mullins CB. Amorphous FeOOH oxygen evolution reaction catalyst for photoelectrochemical water splitting. J Am Chem Soc 2014;136:2843–50.

[69]   Yang X, Chen C, Li J, Zhao G, Ren X, Wang X. Graphene oxide-iron oxide and reduced graphene oxide-iron oxide hybrid materials for the removal of organic and inorganic pollutants. RSC Adv 2012;2:8821–6.

[70]   Morillo D, Uheida A, Pérez G, Muhammed M, Valiente M. Arsenate removal with 3-mercaptopropanoic acid-coated superparamagnetic iron oxide nanoparticles. J Colloid Interface Sci 2015;438:227–34.

[71]   Schwertmann U. Iron Oxides in the Laboratory Preparation and Characterization. 2nd ed. Wiley Online Library; 2008.

[72]   Xu XN, Wolfus Y, Shaulov A, Yeshurun Y, Felner I, Nowik I, et al. Annealing study of Fe2O3 nanoparticles: Magnetic size effects and phase transformations. J Appl Phys 2002;91:4611–6.

[73]   Mondal K, Lorethova H, Hippo E, Wiltowski T, Lalvani SB. Reduction of iron oxide in carbon monoxide atmosphere—reaction controlled kinetics. Fuel Process Technol 2004;86:33–47.

[74]   Justin R, Chen B. Strong and conductive chitosan-reduced graphene oxide nanocomposites for transdermal drug delivery. J Mater Chem B 2014;2:3759–70.

[75]   Habiba K, Makarov VI, Avalos J, Guinel MJF, Weiner BR, Morell G. Luminescent graphene quantum dots fabricated by pulsed laser synthesis. Carbon 2013;64:341–50.

[76]   Peng J, Gao W, Gupta BK, Liu Z, Romero-Aburto R, Ge L, et al. Graphene quantum dots derived from carbon fibers. Nano Lett 2012;12:844–9.

[77]   Zhu S, Zhang J, Tang S, Qiao C, Wang L, Wang H, et al. Surface Chemistry Routes to Modulate the Photoluminescence of Graphene Quantum Dots: From Fluorescence Mechanism to Up-Conversion Bioimaging Applications. Adv Funct Mater 2012;22:4732–40.

[78] Song J-H, Atay T, Shi S, Urabe H, Nurmikko A V. Large enhancement of fluorescence efficiency from CdSe/ZnS quantum dots induced by resonant coupling to spatially controlled surface plasmons. Nano Lett 2005;5:1557–61.

[79] Chen M-L, He Y-J, Chen X-W, Wang J-H. Quantum-dot-conjugated graphene as a probe for simultaneous cancer-targeted fluorescent imaging, tracking, and monitoring drug delivery. Bioconjug Chem 2013;24:387–97.

[80] Pons T, Medintz IL, Sapsford KE, Higashiya S, Grimes AF, English DS, et al. On the quenching of semiconductor quantum dot photoluminescence by proximal gold nanoparticles. Nano Lett 2007;7:3157–64.

[81] Samanta A, Zhou Y, Zou S, Yan H, Liu Y. Fluorescence quenching of quantum dots by gold nanoparticles: a potential long range spectroscopic ruler. Nano Lett 2014;14:5052–7.

[82] Radovic LR, Bockrath B. On the chemical nature of graphene edges: origin of stability and potential for magnetism in carbon materials. J Am Chem Soc 2005;127:5917–27.

[83] Li X-D, Liang X-L, Yue X-L, Wang J-R, Li C-H, Deng Z-J, et al. Imaging guided photothermal therapy using iron oxide loaded poly(lactic acid) microcapsules coated with graphene oxide. J Mater Chem B 2014;2:217–23.

[84] Malyutin AG, Easterday R, Lozovyy Y, Spilotros A, Cheng H, Sanchez-Felix OR, et al. Viruslike Nanoparticles with Maghemite Cores Allow for Enhanced MRI Contrast Agents. Chem Mater 2014;27:327–35.

[85] Gizzatov A, Keshishian V, Guven A, Dimiev AM, Qu F, Muthupillai R, et al. Enhanced MRI relaxivity of aquated Gd3+ ions by carboxyphenylated water-dispersed graphene nanoribbons. Nanoscale 2014;6:3059–63.

[86] Chen Y, Xu P, Shu Z, Wu M, Wang L, Zhang S, et al. Multifunctional Graphene Oxide-based Triple Stimuli-Responsive Nanotheranostics. Adv Funct Mater 2014;24:4386–96.

[87] Gupta AK, Gupta M. Cytotoxicity suppression and cellular uptake enhancement of surface modified magnetic nanoparticles. Biomaterials 2005;26:1565–73.

[88] Wang K, Ruan J, Song H, Zhang J, Wo Y, Guo S, et al. Biocompatibility of Graphene Oxide. Nanoscale 2010:1–8.

[89] Justin R, Chen B. Body temperature reduction of graphene oxide through chitosan functionalisation and its application in drug delivery. Mater Sci Eng C 2014;34:50–3.

[90] Kim J, Kim Y-R, Kim Y, Lim KT, Seonwoo H, Park S, et al. Graphene-incorporated chitosan substrata for adhesion and differentiation of human mesenchymal stem cells. J Mater Chem B 2013;1:933–8.

[91] Liu H-W, Hu S-H, Chen Y-W, Chen S-Y. Characterization and drug release behavior of highly responsive chip-like electrically modulated reduced graphene oxide–poly(vinyl alcohol) membranes. J Mater Chem 2012;22:17311–20.

[92] Korsmeyer RW, Gurny R, Doelker E, Buri P, Peppas NA. Mechanisms of solute release from porous hydrophilic polymers. Int J Pharm 1983;15:25–35.

[93] Pandey H, Parashar V, Parashar R, Prakash R, Ramteke PW, Pandey AC. Controlled drug release characteristics and enhanced antibacterial effect of graphene nanosheets containing gentamicin sulfate. Nanoscale 2011;3:4104–8.

[94] Ma D, Lin J, Chen Y, Xue W, Zhang L-M. In situ gelation and sustained release of an antitumor drug by graphene oxide nanosheets. Carbon N Y 2012;50:3001–7.

[95] Zhang R, Hummelgård M, Lv G, Olin H. Real time monitoring of the drug release of rhodamine B on graphene oxide. Carbon N Y 2011;49:1126–32.

[96] Yang K, Wan ḰJ, Zhang ḰS, Zhang Y, Lee S, Liu Z. In Vivo Pharmacokinetics, Long-Term Biodistribution, and Toxicology of PEGylated Graphene in Mice. ACS Nano 2010;5:516–22.

[97] Jaque D, Martínez Maestro L, del Rosal B, Haro-Gonzalez P, Benayas A, Plaza JL, et al. Nanoparticles for photothermal therapies. Nanoscale 2014;6:9494–530.

[98] Liu X, Tao H, Yang K, Zhang S, Lee S-T, Liu Z. Optimization of surface chemistry on single-walled carbon nanotubes for in vivo photothermal ablation of tumors. Biomaterials 2011;32:144–51.

[99] Stern JM, Stanfield J, Kabbani W, Hsieh J-T, Cadeddu JA. Selective prostate cancer thermal ablation with laser activated gold nanoshells. J Urol 2008;179:748–53.

[100] Brunner TJ, Wick P, Manser P, Spohn P, Grass RN, Limbach LK, et al. In vitro cytotoxicity of oxide nanoparticles: comparison to asbestos, silica, and the effect of particle solubility. Environ Sci Technol 2006;40:4374–81.

[101] Y. Zhang, N. Kohler, and M. Zhang, "Surface modification of superparamagnetic magnetite nanoparticles and their intracellular uptake.," Biomaterials, vol. 23, no. 7, pp. 1553–1561, 2002.

[102] Li Y, Lu W, Huang Q, Huang M, Li C, Chen W. Copper sulfide nanoparticles for photothermal ablation of tumor cells. Nanomedicine 2010;5:1161–71.

[103] Zhou M, Zhang R, Huang M, Lu W, Song S, Melancon MP, et al. A chelator-free multifunctional [64Cu]CuS nanoparticle platform for simultaneous micro-PET/CT imaging and photothermal ablation therapy. J Am Chem Soc 2010;132:15351–8.

[104] Xu Y, Qin Y, Palchoudhury S, Bao Y. Water-soluble iron oxide nanoparticles with high stability and selective surface functionality. Langmuir 2011;27:8990–7.

[105] Lu Y, Kong H, Wen F, Zhang S, Zhang X. Lab-on-graphene: graphene oxide as a triple-channel sensing device for protein discrimination. Chem Comm 2013;49:81–3.

[106] Kalia YN, Naik A, Garrison J, Guy RH. Iontophoretic drug delivery. Adv Drug Deliv Rev 2004;56:619–58.